Non-parametric spectral modelling of source parameters, path attenuation and site effects from broad-band waveforms of the Alborz earthquakes (2005–2017)

Somayeh Ahmadzadeh,[1] G. Javan Doloei,[1] Stefano Parolai[2] and Adrien Oth[3]

[1] *International Institute of Earthquake Engineering and Seismology (IIEES), Tehran, 1953714453, Iran. E-mail: javandoloei@iiees.ac.ir*
[2] *Istituto Nazionale di Oceanografia e di Geofisica Sperimentale – OGS, 34010 Sgonico (TS), Italy*
[3] *European Center for Geodynamics and Seismology, 7256 Walferdange, Luxembourg*

SUMMARY

S-wave spectral amplitudes from 312 crustal earthquakes recorded at the Iranian National Broadband Seismic Network in the Alborz region between 2005 and 2017 are analysed in order to evaluate earthquake source parameters, path attenuation and site amplification functions using the non-parametric generalized inversion technique (GIT). We exploit a total number of 1117 seismograms with M_L 3–5.6 in the frequency range 0.3–20 Hz. The evaluated non-parametric attenuation functions decay uniformly with distance for the entire frequency range and the estimated *S*-wave quality factor shows low *Q* values with relatively strong frequency dependence. We assume the omega-square source model to retrieve earthquake source parameters from the inverted source spectra. The obtained stress drops range from 0.02 to 16 MPa with a mean value of 1.1 MPa. Stress drop and radiated energy show fairly self-similar scaling with seismic moment over the available magnitude range; however, the magnitude range of this study is too narrow to draw a definite conclusion on source scaling characteristics. The obtained moment magnitude M_w and the local magnitude M_L are linearly correlated and approximately equivalent in the range of M_w 3–4. For larger events, M_w generally underestimates M_L by about 0.1–0.5 magnitude units. The estimated site amplification functions for horizontal component (GIT H) are nearly flat with no obvious pre-dominant frequency peaks for most stations, as expected for the sites of permanent broad-band seismic stations located on rock, though a few stations show amplification peaks from 1 to 8 Hz, with a maximum amplification of about a factor of 7 with respect to the reference site. The evaluated site responses for the vertical components present remarkable amplification or deamplification, leading to differences of the H/V amplitude levels in comparison with the GIT H amplification curves. The results of this study provide a valuable basis for predicting appropriate ground motions in a context of seismic hazard assessment.

Key words: Earthquake source observations; Seismic attenuation; Site effects; Body wave; Wave propagation.

1 INTRODUCTION

Located along the Alpine–Himalayan seismic belt, the Iran plateau is characterized by severe seismic activity with frequent devastating earthquakes occurring in the whole country. The Iran plateau has been divided into different seismotectonic zones with distinct geologic, seismic and tectonic characteristics (Stocklin 1968; Berberian 1976; Nowroozi 1976; Alavi 1996; Mirzaei *et al.* 1998). The region under study is located in Alborz, one of the major seismotectonic provinces of Iran. The Alborz mountain range is a seismically active fold and thrust sinuous range along the southern coast of the Caspian Sea in northern Iran. The range is narrow, with 100 km width and about 600 km length, and accommodates relative motion between

the South Caspian Basin and Central Iran. GPS measurements of Vernant *et al.* (2004) showed 5 ± 2 mm yr^{-1} of north–south shortening and a left-lateral shear across the Alborz at a rate of 4 ± 2 mm yr^{-1}. The crustal thickness beneath the Central Alborz is about 55–58 km (Abbassi *et al.* 2010; Radjaee *et al.* 2010) and decreases to about 46–48 km north and south of the Alborz Mountains (Doloei & Roberts 2003; Radjaee *et al.* 2010). In contrast to the interplate Zagros region with rapid uplift and frequent moderate-sized earthquakes, Alborz is characterized by lower slip rates, large-magnitude and shallow earthquakes accompanied by surface faulting (Berberian & Yeats 1999). Many catastrophic earthquakes occurred during the historic and instrumental time period (e.g. Rudbar–Tarom earthquake of 1990 with M_w 7.3 and Baladeh earthquake of 2004 with

M_w 6.2) in the Alborz region (Ambraseys & Melville 1982; Berberian *et al.* 1992; Tatar *et al.* 2007; Donner *et al.* 2013). The latest destructive event occurred on 2004 May 28 near Baladeh, about 70 km north of Tehran. Most focal mechanism solutions as well as structural observations in the Alborz show either reverse faulting or left-lateral strike-slip on faults parallel to the regional strike of the belt (Jackson *et al.* 2002; Allen *et al.* 2003; Donner *et al.* 2014). The Alborz region contains several active faults including thrust and strike-slip faults (e.g. Khazar, North Alborz, Mosha, North Tehran, Eshtehard, Taleghan, etc.) along the length of the range changing from an ENE strike in the east to a WNW strike in the west (Allen *et al.* 2003). Several populated and important cities, including the capital Tehran (with more than 10 million residents), are located in the Alborz region. Thus, dense populations of the urban areas in addition to the tectonic setting of the Alborz emphasize the significance of the seismic risk and hazard assessments in the region. In order to obtain precise ground motion predictions, accurate estimations of seismic sources and path attenuation characteristics are required in addition to the knowledge on near surface site amplification effects. A common approach to separate source, site and path effects from seismic observations is the generalized inversion technique (GIT), first introduced by Andrews (1986), which has been frequently used and developed in various studies worldwide (Parolai *et al.* 2000; Dutta *et al.* 2003; Tsuda *et al.* 2010; Oth *et al.* 2011; Castro *et al.* 2013; Pacor *et al.* 2016 among others). On the Iran plateau, a limited number of studies have been carried out to investigate region specific seismic source, path and site effects for the major seismotectonic provinces in recent years. Among few researches for the Alborz region, Motazedian (2006) analysed 259 accelerograms of 22 earthquakes to examine propagation characteristics of ground motions in northern Iran. Then, using the stochastic point-source and finite-fault approaches, source parameters have been estimated. The only available study that implemented the parametric GIT method for the Alborz region was performed by Zafarani *et al.* (2012). They analysed 228 *S*-wave amplitude spectra of 29 earthquakes sparsely recorded at 81 strong-motion stations to obtain source parameters, site responses and *S*-wave attenuation (Q_S). However, the limited ray coverage used in their study resulted in significant uncertainties. Hence, considering the hazardous seismically active area of the Alborz region, performing a comprehensive work based on a rich and reliable database is of outmost importance.

In this study, we apply the non-parametric GIT to an extensive 12-yr broad-band seismogram data set, densely recorded in the study area, in order to simultaneously evaluate source parameters, site and path effects in the Alborz region. Earthquake source parameters including stress drop and *S*-wave radiated energy are investigated from inverted source spectra and the source scaling relations are studied as well. We evaluated the *S*-wave frequency-dependent quality factor from the non-parametric attenuation functions and compared the results with other studies in Iran. Finally, estimated site responses using GIT are compared with horizontal to vertical (H/V) spectral ratios for 10 Iranian National Broadband Seismic Network stations used in this study.

2 DATA SET

More than 800 earthquakes with magnitudes larger than 3 were recorded by the Iranian National Broadband Seismic Network (BIN) in the Alborz region and nearby area from January 2005 to August 2017. The network started its activity from 1998 with four stations, and the number of stations has been increased to 28 by the end of

2017. All stations are equipped with Güralp CMG-3T broad-band seismometers with sampling rates of 50 Hz. For the purpose of this study we used all available 10 seismic stations located within the study area to provide a good coverage on seismicity of the Alborz region. A subset of 499 events recorded at least at six stations was selected with well-constrained locations (location error < 3 km and GAP < 180°) and epicentral distances less than 200 km and $M_L \geq 3$. The M_L values are obtained from the International Institute of Earthquake Engineering and Seismology (IIEES) Bulletin (http://www.iiees.ac.ir/en/eqcatalog/) that is calculated based on the relation of Hutton & Boore (1987).

In order to obtain reliable results in the inversion process, only stations and earthquakes with at least three recordings were considered. Hence the final database consists of 1117 records from 312 events which most of them are recorded by more than four stations.

Fig. 1 shows the location map of the 312 selected events as well as the 10 stations of the Iranian National Broadband Seismic Network used in this study. The source-station travel paths displayed indicate excellent coverage of the area within the network. The magnitudes of the selected events versus hypocentral distance and focal depth are presented in Fig. 2. The recorded earthquakes span the magnitude range M_L 3–5.6. The hypocentral distances vary from 17 to 200 km and the focal depths of the events are shallower than 30 km.

The raw records were corrected for instrumental response and a time window of 10 s length was selected on the horizontal components starting 1 s before the *S*-wave arrival. Each selected window is tapered with a 5 per cent cosine window. The acceleration Fourier amplitude spectra (FAS) have been computed and smoothed using the Konno & Ohmachi (1998) windowing function with $b = 20$ and sampled at 30 frequency points equidistant on log scale between 0.3 and 20 Hz. Pre-event noise windows with the same length as the *S*-wave windows were considered to evaluate the signal-to-noise ratio (SNR) and only records with an SNR higher than 3 were retained at each frequency point. Therefore, the number of selected spectral amplitudes applied for the inversion is slightly different at some frequency points and vary from 905 to 1117 in the considered frequency range. Finally, the root-mean-square of two horizontal components ($\sqrt{(NS^2 + EW^2)/2}$) is used for the spectral analysis. Fig. 3 shows two examples for the above-mentioned data processing.

3 METHODS

3.1 Spectral inversion approach

In order to separate the source spectra, attenuation characteristics and site responses from the observed *S*-wave amplitude spectra we apply the commonly used non-parametric GIT following Castro *et al.* (1990). Here we present a brief description of the GIT method and refer the reader to the literature for further details (e.g. Andrews 1986; Parolai *et al.* 2004a; Drouet *et al.* 2005; Edwards *et al.* 2008; Bindi *et al.* 2017; Picozzi *et al.* 2019).

The Fourier amplitude spectra of ground motion can be written as

$$U_{ij}\left(f, M_i, R_{ij}\right) = S_i\left(f, M_i\right).A\left(f, R_{ij}\right).G_j\left(f\right), \tag{1}$$

where $U_{ij}(f, M_i, R_{ij})$ is the observed FAS at the *j*th station from the *i*th earthquake with magnitude M_i; R_{ij} is the hypocentral distance; $S_i(f, M_i)$ represents the source spectrum of the *i*th event; $A(f, R_{ij})$ stands for the attenuation along the travel path, and $G_j(f)$ denotes the site response function of the jth station. Taking the logarithm of
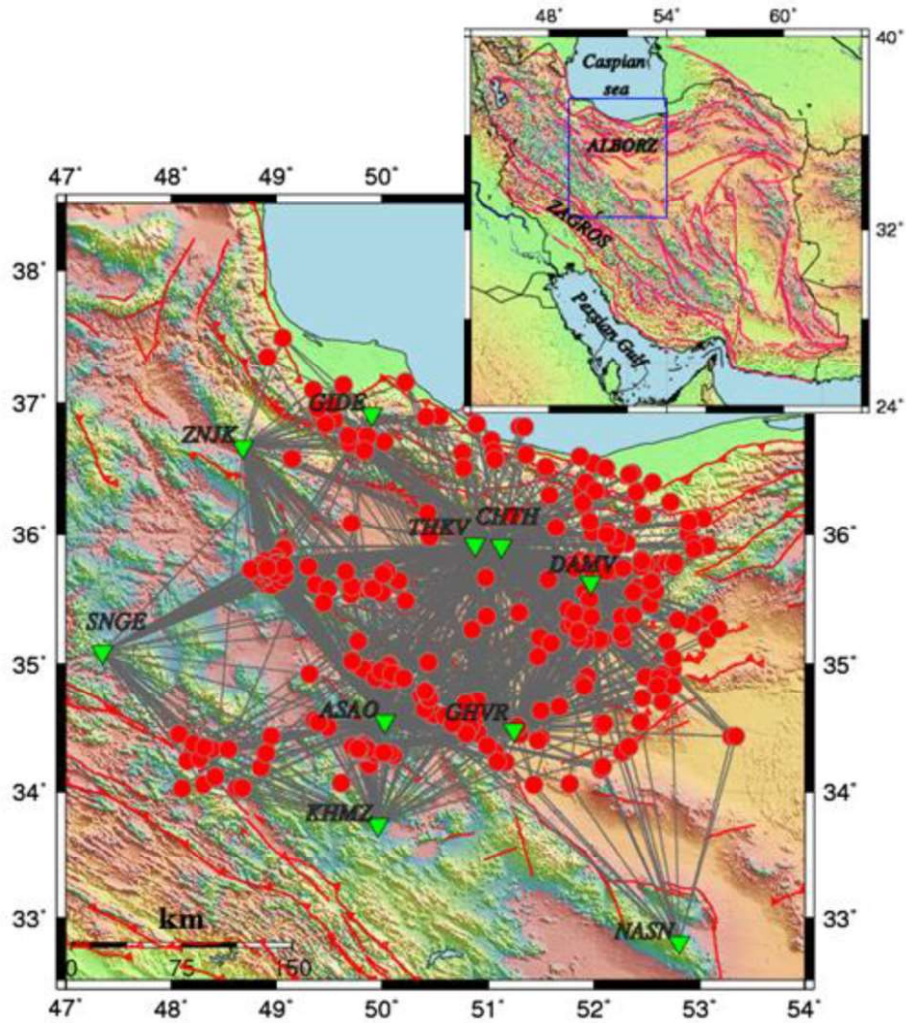
Figure 1. Epicentres of 312 selected earthquakes (circles) occurred during 2005–2017 in the Alborz region. Inverse triangles indicate the location of 10 broad-band seismic stations of BIN. The source-station ray paths are shown as grey lines. The study area is shown with a box in the top inset within Iran plateau.
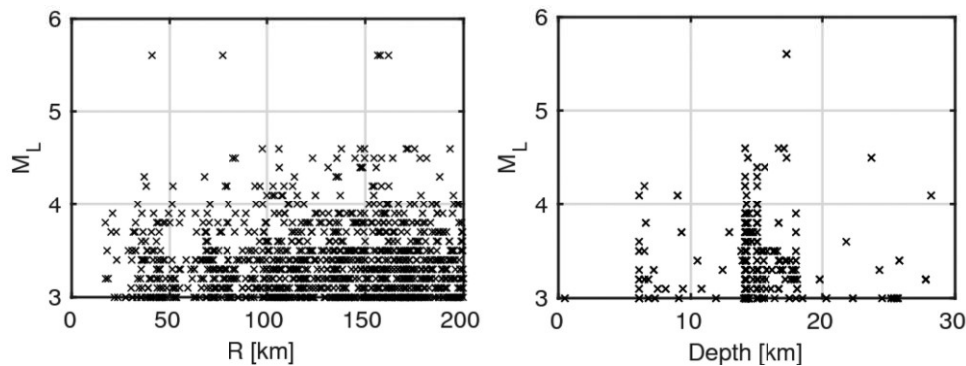

Figure 2. Distribution of earthquake magnitude (M_L) versus hypocentral distance (left) and depth (right).

both sides, eq. (1) turns into a linear problem:

$$\log_{10} U_{ij}\left(f, M_i, R_{ij}\right) = \log_{10} S_i(f, M_i) + \log_{10} A(f, R_{ij})$$
$$+ \log_{10} G_j(f). \quad (2)$$

Considering all recordings, eq. (2) constitutes a linear system of equations $\mathbf{Ax} = \mathbf{b}$ where $\mathbf{b}$ is the data vector containing the observed spectral amplitudes, $\mathbf{x}$ denotes the model vector and $\mathbf{A}$ is the system matrix relating them. We resolve this system of equations in one step using the Least Squares QR (LSQR) algorithm (Paige & Saunders 1982) to calculate the source spectra, path attenuation characteristics and site amplification functions, simultaneously. The inversion can be implemented using either a parametric or non-parametric approach. In contrast to the parametric method, the attenuation
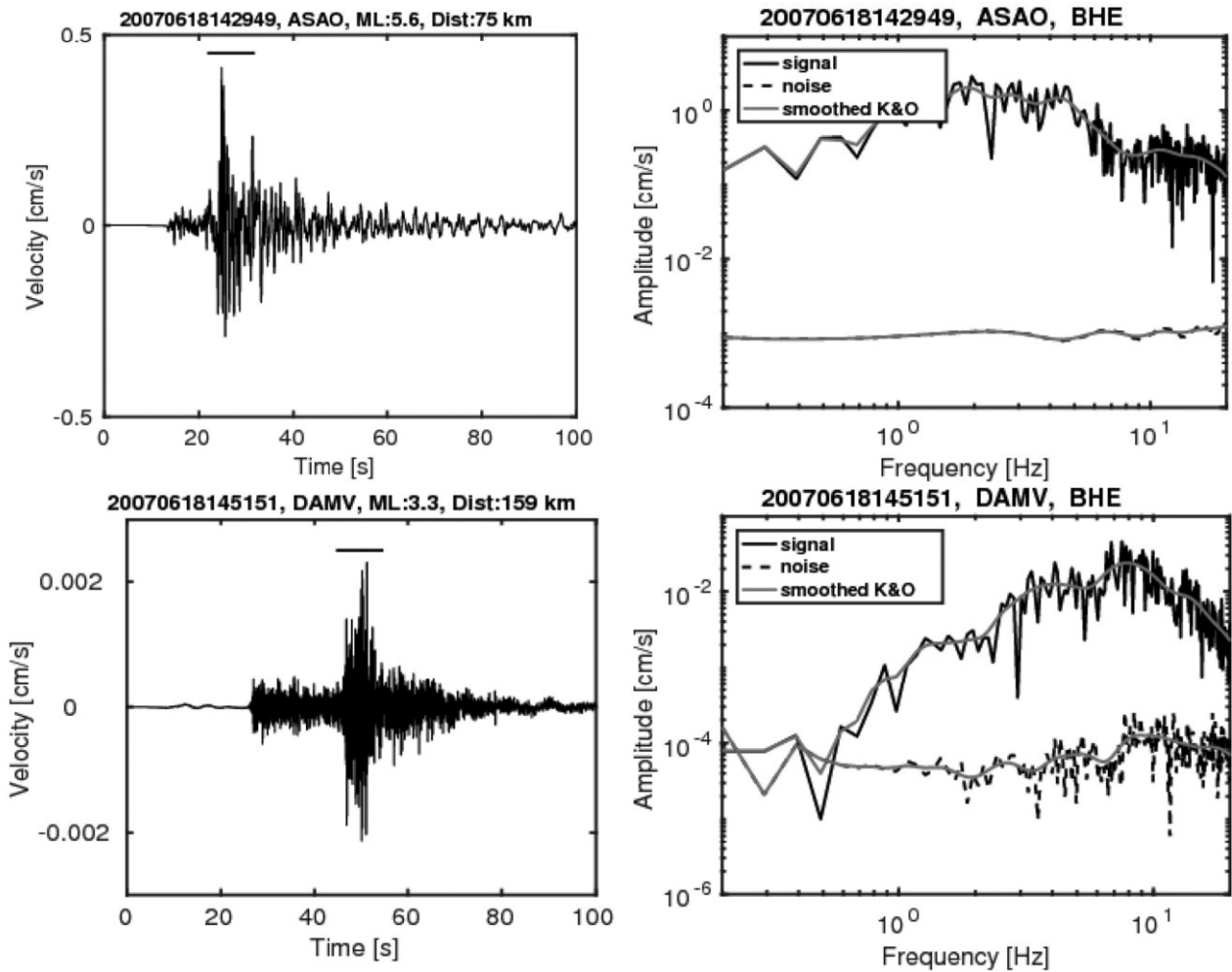
Figure 3. Two instrument-corrected EW component velocity seismograms at stations ASAO and DAMV (left) and calculated acceleration FAS of the seismograms (right). The smoothed amplitude spectra using the konno-Ohmachi filter with $b = 20$ are indicated with grey lines for both signal and noise spectra. The selected *S*-wave window to evaluate the FAS is indicated with the black bar over the seismograms.
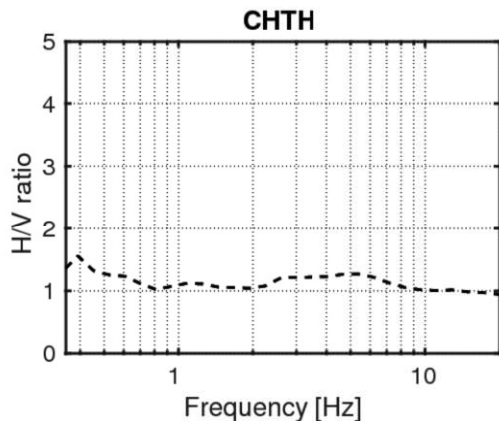

Figure 4. The H/V spectral ratio calculated from the observed spectra at station CHTH. The spectral ratio is considerably flat and close to one at all frequencies.

operator $A(f,R_{ij})$ is not a pre-defined function in the non-parametric scheme (it is only constrained to be a smooth function with distance), which enables to assess the potential complexity of attenuation characteristics without imposing an *a priori* parametric model.

The non-parametric attenuation functions contain all attenuation effects like geometrical spreading, anelasticity and scattering, and it takes the value of 1 at a given reference distance R_0, which is set to 17 km in this study.

In order to resolve the undetermined degree of freedom as noted by Andrews (1986), a reference condition either for at least one appropriate source or site has to be set. A common approach is to constrain the site response of one rock site or average of several rock stations to be equal to one, irrespective of frequency. Since all site amplification and source spectra resulting from the inversion are relative to the imposed constraint, selecting an appropriate reference condition is of utmost importance. Located on the southern flank of the central Alborz Mountain, station CHTH is deployed on monzodiorite bedrock outcrop and has an appropriate geological condition. Moreover, this station represents absolutely flat and close to unity response at all frequencies based on H/V analysis (Fig. 4). Hence, CHTH is an appropriate choice as reference station.

3.2 Bootstrap analysis

In order to evaluate the stability of the inversion results, a bootstrap analysis is applied at each frequency point following Parolai *et*
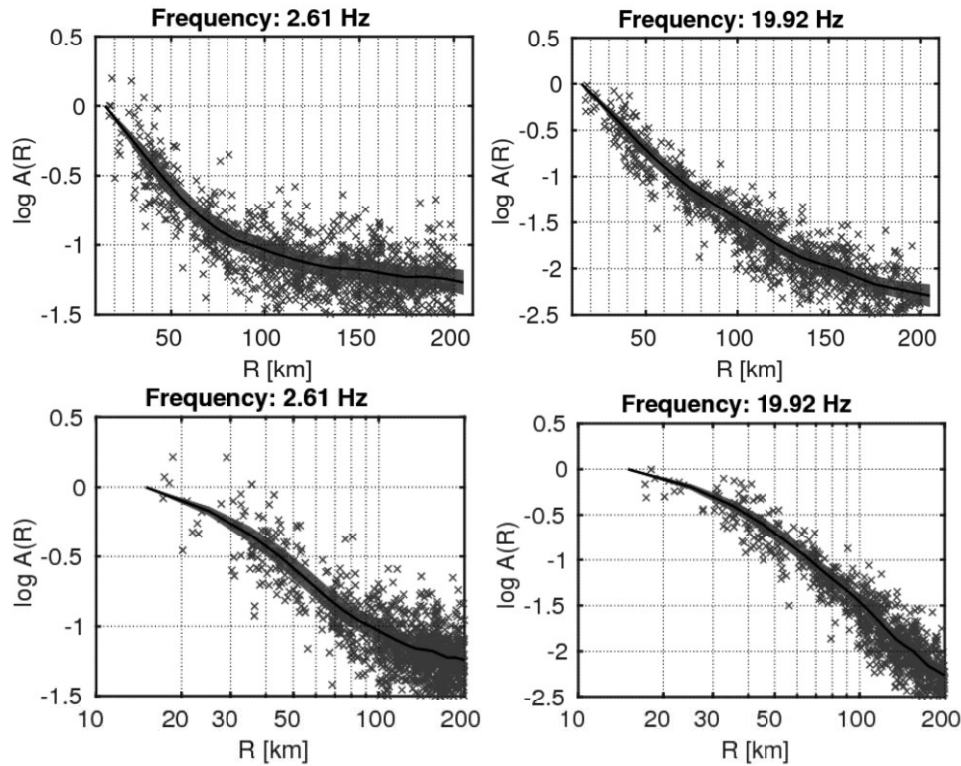
Figure 5. Top: non-parametric attenuation functions for two selected frequencies. The grey shaded area denotes one standard deviation calculated by bootstrap analysis around the mean. The observed spectral amplitudes are indicated as black crosses. Bottom: the same as top but in logarithmic scale on the *x*-axis.
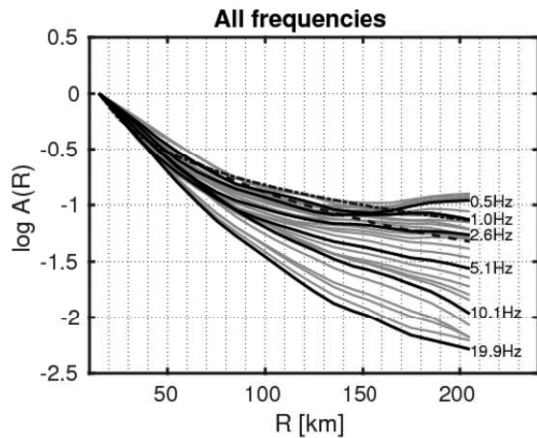

Figure 6. Non-parametric attenuation functions versus hypocentral distance for all 30 frequencies. R^{-1} (dash-dotted line) and the piece wise R^{-b} (dashed line) curves are displayed for comparison. Note that $\log A(f,R) = 0$ at the reference distance $R_0 = 17$ km.

al. (2000, 2004a). The bootstrap method (Efron 1979) implements repeated inversions using bootstrap data obtained by randomly resampling *n* times the original data set. Thus, assuming an original matrix of *N* data points including *N* spectral amplitudes at each frequency, we perform inversions for a matrix of the same size as the original one, consisting of rows selected randomly from the initial matrix. A certain row in each bootstrap sample can either be chosen several times or never. However, the rows including the previously mentioned constraints are involved in each bootstrap sample. The statistics of the bootstrap replications are computed for each model parameter. We performed 100 bootstrap inversions at each frequency and evaluated the mean and standard deviation of

these 100 iterations for model parameters to assess the stability of the results.

3.3 H/V spectral ratio

The horizontal to vertical (H/V) spectral ratio technique has been extensively used to evaluate local site amplification effects. The H/V technique was originally proposed by Nakamura (1989) to interpret ambient noise measurements. Lermo & Chavez-Garcia (1993) applied this technique to the *S* waves of earthquake data. Since then, the H/V has been used in several studies worldwide (Parolai *et al.* 2004a,b; Sokolov *et al.* 2005; Oth *et al.* 2009; Pilz *et al.* 2009; Ahmadzadeh *et al.* 2017) for the assessment of site responses.

In general, comparison of site amplification functions estimated with different approaches (Bonilla *et al.* 1997; Parolai *et al.* 2004a; Haghshenas *et al.* 2008) reveals that the H/V method which provides comparable estimates of the fundamental resonance frequency of a site however usually underestimates the level of amplification as compared with for instance the GIT technique.

We estimate the site amplification functions using the GIT method for the Alborz data set and compare the results with those calculated by means of the H/V spectral ratios directly from the observed spectra to inspect the relation between different site amplification functions.

4 SPECTRAL INVERSE MODELLING RESULTS

Implementing a one-step non-parametric GIT inversion to the observed spectral amplitudes, the path attenuation, source spectra and site responses are evaluated simultaneously. The results are presented and described in details as the following procedures.
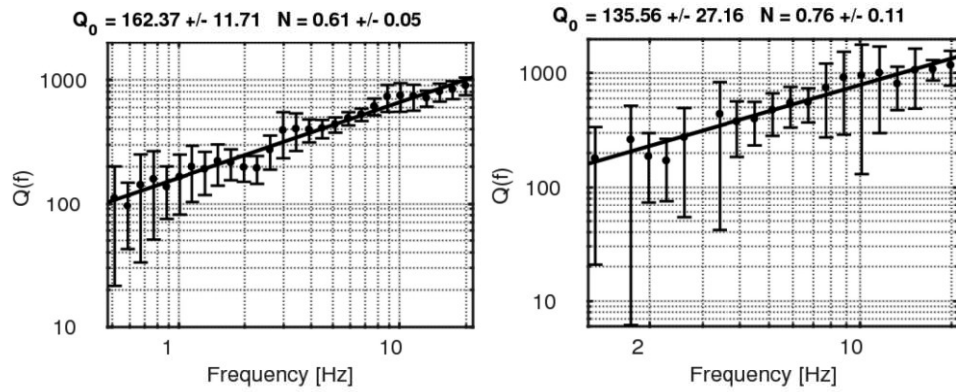
Figure 7. The solid black line indicates the obtained $Q(f)$ model from the analysis of the attenuation functions from GIT inversion for single decay geometrical spreading (left) and bi-linear geometrical model (right). The individual Q values derived at each given frequency are denoted by dots and error bars. Please note that due to different approaches considered for geometrical spreading function $G(R)$ the obtained quality factors are different in two figures so the sampled frequencies are not exactly the same.
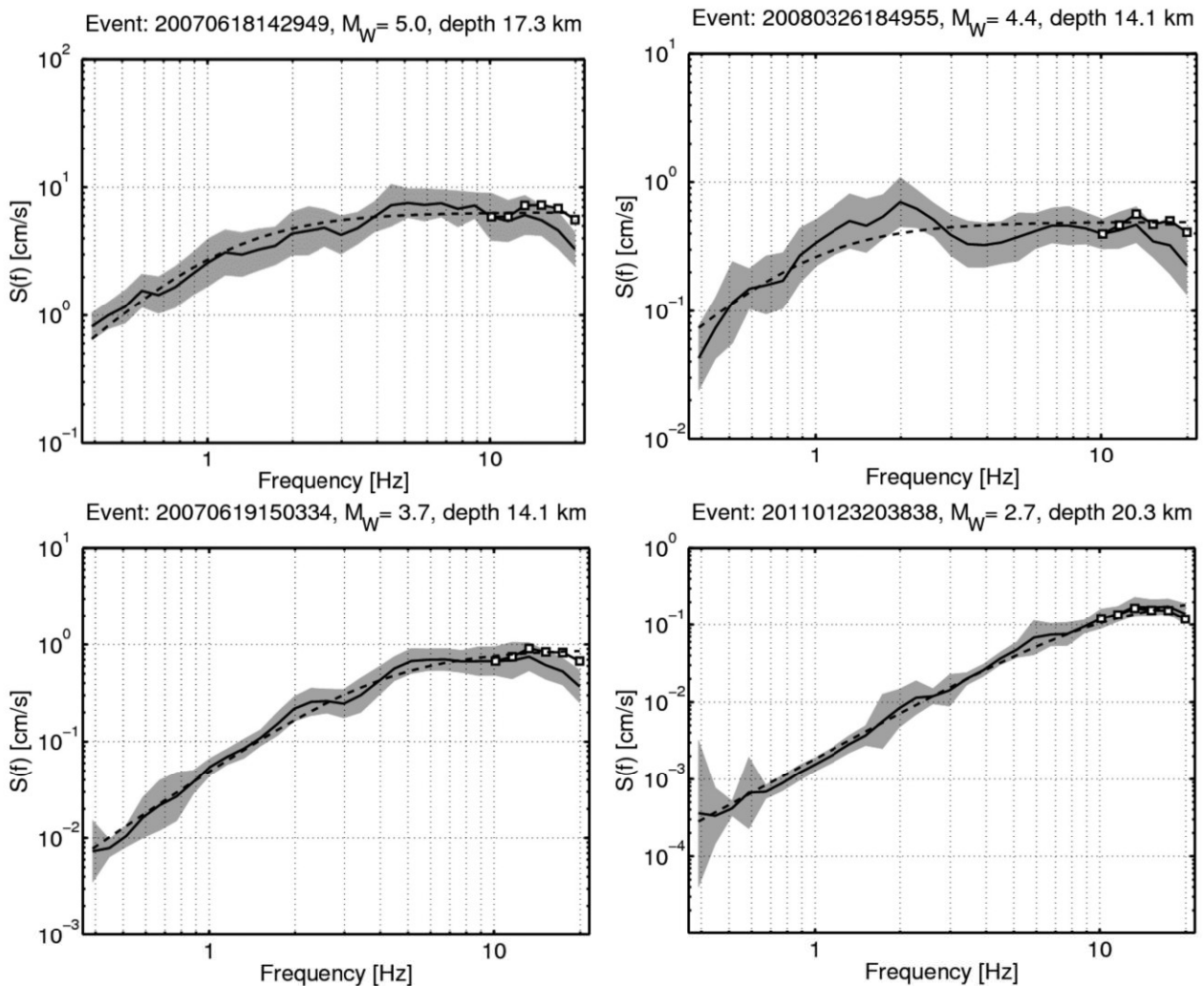

Figure 8. Four examples of acceleration source spectra derived from the GIT inversion (solid black lines) with related standard deviation (shaded area). The best fitted ω^2 model is indicated by dashed lines. The white square trend indicates the high-frequency κ correction at frequencies larger than 10 Hz.

4.1 Path attenuation characteristics

The obtained non-parametric attenuation functions for two selected frequencies together with the observed spectral amplitudes after removing source and site effects are shown in Fig. 5. The hypocentral distance of the data ranging from 17 to 200 km is discretized into 20 bins of 10 km width and the attenuation function is computed in each bin. The reference distance is selected as $R_0 = 17$ km. The attenuation curves decay uniformly with distance and describe the
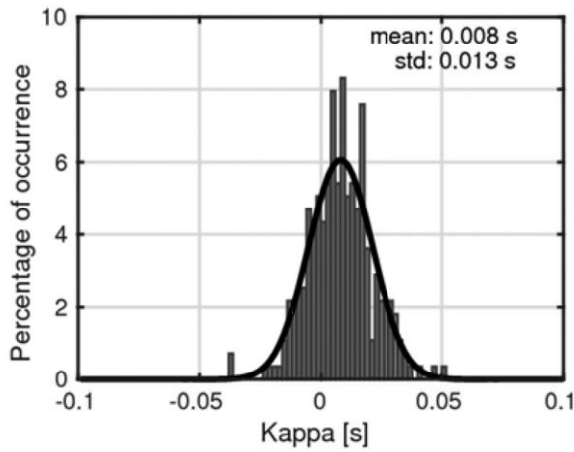
Figure 9. κ distribution from the analysis of high-frequency part of the inverted source spectra for $f > 10$ Hz. The obtained κ values are almost normally distributed.

corrected spectral amplitudes quite well. The small value of the standard deviation estimated from the bootstrap analysis is shown as grey shaded area around the mean value indicating that the attenuation functions are well constrained. To better capture the changes in the rate of attenuation with distance in the first 50 km the attenuation functions for two frequencies (2.61 and 19.92 Hz) are also depicted in the bottom of Fig. 5 in logarithmic scale. In this range of distances, the effect of the intrinsic attenuation is expected to be small and the transmission is playing a major role.

Fig. 6 shows the attenuation functions for all 30 frequency points between 0.3 and 20 Hz. The functions generally decay monotonically with distance for all frequencies with a rapid decay for the first 100 km. The attenuation functions almost decay the same as $1/R$ function up to 70 km. However, for larger distances the attenuation functions attenuate more quickly than $1/R$ curve for the entire frequency range.

The obtained non-parametric attenuation functions can be described in terms of geometrical spreading and apparent shear wave quality factor by the following relation (e.g. Boore 1983):

$$A\ (f,\ R) =\ G\ (R)\exp\left[-\frac{\pi f\ (R - R_0)}{Q\ (f)\ V_\mathrm{s}}\right], \tag{3}$$

where $G(R)$ is the geometrical spreading function, R is the hypocentral distance in km, R_0 is the reference distance for the fit, $Q(f)$ denotes the apparent shear wave quality factor and Vs is the shear wave velocity. Note that due to crustal complexities, we only consider the attenuation functions in the distance range 17–100 km to derive shear wave quality factor. Since a trade-off exists for solving eq. (3) to determine geometrical spreading and $Q(f)$ together, we fix the geometrical spreading function and evaluate the frequency dependence of quality factor. To this end we consider two approaches for the geometrical spreading: (1) a single decay curve with $G(R) = (R_0/R)^b$ for a fix exponent value $b = 1$ and (2) a piece-wise geometrical spreading model for different distance ranges.

Then these models are applied to correct the obtained attenuation functions and to extract the frequency-dependent attenuation model including the S-wave quality factor contribution.

We fit a bi-linear geometrical spreading model with a hinge distance at 70 km to a set of low-frequency curves ranging from 0.6 to 1 Hz where the effect of the anelastic attenuation is negligible. Thereafter under the assumption that the geometrical spreading is

frequency independent, the adopted model could be applied to all frequencies to obtain the apparent quality factor.

Following Pacor *et al.* (2016), we propose a piece-wise geometrical spreading model which leads to eq. (4) based on the best least-squares solution:

$$G\ (R) = \begin{cases} \left(\frac{R_0}{R}\right)^{b_1} & \text{for } R < 70 \text{ Km} \\ \left(\frac{R_0}{70}\right)^{b_1}\left(\frac{70}{R}\right)^{b_2} & \text{for } 70 \text{ Km} \le\ R < 100 \text{ Km} \end{cases} \tag{4}$$

where the geometrical spreading exponents b_1 and b_2 are 1 and 1.4, respectively. This model represents more rapid attenuation than R^{-1} up to 100 km that is also observed by other studies for short and intermediate distances worldwide (Yenier & Atkinson 2015; Bindi *et al.* 2017), which means that the effect of the intrinsic and transmission attenuation becomes larger when the distances increase and many cycles are done by each frequency.

This way, the non-parametric attenuation function $A(f,R)$ is corrected for both single decay model and bi-linear geometrical spreading. Then the frequency-dependent quality factor ($Q(f)$) is determined from the slope of a least-squares regression to $\log A(f,r)$–$\log G(r)$ versus distance. Finally, a power function of the form $Q(f) = Q_0 f^{N}$ is fitted to the estimated $Q(f)$ values to determine Q_0 and N through least-squares inversion as well. It should be noted that by this fitting procedure, the obtained $Q(f)$ results are dependent on the geometrical spreading models considered here, which should in particular be taken into account in the comparison with other studies. The values of $Q(f)$ estimated for all frequencies and the least-squares fit of the power function are shown in Fig. 7. The frequency-dependent quality factor is well approximated for both approaches with the following relations for single decay model and bi-linear model, respectively:

$$Q\ (f) = 162.37\ f^{0.61} \tag{5}$$

$$Q\ (f) = 135.56\ f^{0.76} \tag{6}$$

The obtained Q models for both geometrical spreading functions are nearly identical; however, the second one shows more scattered values at low frequencies. In the case of bi-linear model the geometrical spreading function $G(R)$ is partitioned into two pieces for distances less than 70 and 70–100 km. This division of our input data set leads to decrease in number of hypocentral bins for each part and so increasing errors in comparison with single decay model are expected.

The evaluated Q models indicate strong frequency dependence of the propagation and high attenuation characteristics in the Alborz region. It should be noted that since we are working with large distances, the obtained Q from the analysis of the data set leads to an average apparent attenuation. Our result is similar to the other studies for this region and other tectonically active regions of Iran (Motazedian 2006; Motaghi & Ghods 2012; Ahmadzadeh *et al.* 2017) and the world (Bindi *et al.* 2006; Castro *et al.* 2008; Parolai *et al.* 2010; Oth *et al.* 2011; Wang *et al.* 2018 among others).

As mentioned earlier, the non-parametric attenuation function $(A(f,r))$ contains all attenuation characteristics of seismic waves along the travel path including intrinsic and scattering attenuation. Hence the estimated apparent quality factor also includes aforementioned effects. Though the obtained apparent quality factor is frequency dependent, we cannot directly infer the frequency dependence of the intrinsic Q from the latter.
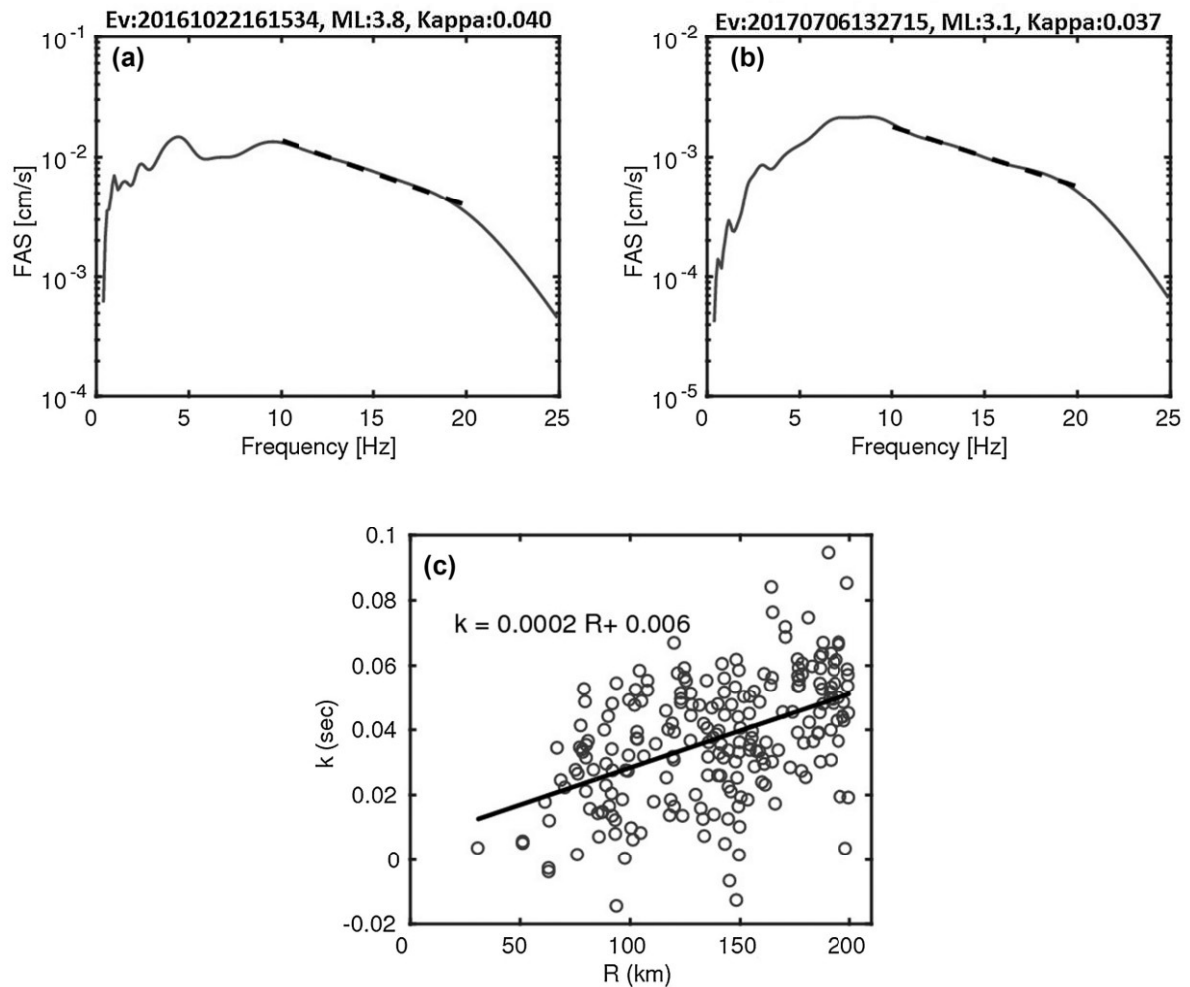
Figure. 10. (a and b) Log-linear plot of Fourier amplitude spectra (solid line) and linear fit (dashed line) for two observed spectra at station CHTH. (c) The distribution of kappa values versus distance for average horizontal components at station CHTH. The solid line indicates the best least-squares fit.

4.2 Source spectra

The isolated non-parametric source terms, $S_i(f, M_i)$, represent the acceleration source spectra at the adopted reference distance R_0. Since we did not make any special assumption for the functional form of the source spectra, they can in principle be interpreted in terms of any appropriate source model. As can be seen from Fig. 8, the inverted source spectra show an increase at low frequencies almost proportional to ω^2 and tend to flatten at high frequencies consistent with the omega-square Brune (1970, 1971) source model. Accordingly, we fit the ω^2 source model to the inverted non-parametric acceleration source spectra to derive earthquake source parameters including corner frequency, f_c and seismic moment, M_0 using the following equation:

$$S(f) = (2\pi f)^2 \frac{R^{\theta\varphi} V F}{4\pi \rho V_s^3 R_0} M(f) \quad \text{with} \quad M(f) = \frac{M_0}{1 + (f/f_c)^2}$$

(7)

where $R^{\theta\varphi}$ denotes the average shear wave radiation pattern set to 0.55 (Boore & Boatwright 1984), $V = 1/\sqrt{2}$ accounts for the partition of total S-wave energy into two horizontal components, $F = 2$ is free surface amplification, $\rho = 2.8$ g cm^{-3} is the density, $V_s = 3.6$ km s^{-1} is the shear wave velocity in the vicinity of the source region, R_0 stands for the reference distance and $M(f)$

represents the moment rate spectrum. Four examples of inverted source spectra (solid black lines, with standard deviation from 100 bootstrap samples as grey shading) as well as an ω^2 source model (dashed lines) fitted to the spectra using nonlinear least squares are shown. In general, the estimated source spectra are very stable considering the standard deviations obtained from 100 bootstrap analysis and the spectra are excellently fitted by ω^2 model. The majority of spectra in Fig. 8 show slight decay at high frequencies. The observed high-frequency κ decay originates from the fact that κ decay was not accounted for in the reference site constraint so that it can be shifted into the estimated source spectra as discussed by Oth *et al.* (2011).

The high-frequency source slopes are often considered to be linked to site effects in view of the near surface attenuation that is characterized as an exponential of the form $\exp(-\pi\kappa f)$ (Anderson & Hough 1984). Nevertheless, some studies have shown that there is a dependency of the high-frequency diminution to source parameters like magnitude and focal mechanism (Petukhin *et al.* 1999; Purvance & Anderson 2003; Kilb *et al.* 2012) in addition to path and distance dependencies considered in other studies (Anderson 1991; Fernández-Heredia *et al.* 2012). Since the site effects is the most widely accepted point of view and effect of source and distance have variable importance depending on the region and study (Ktenidou *et al.* 2014) we
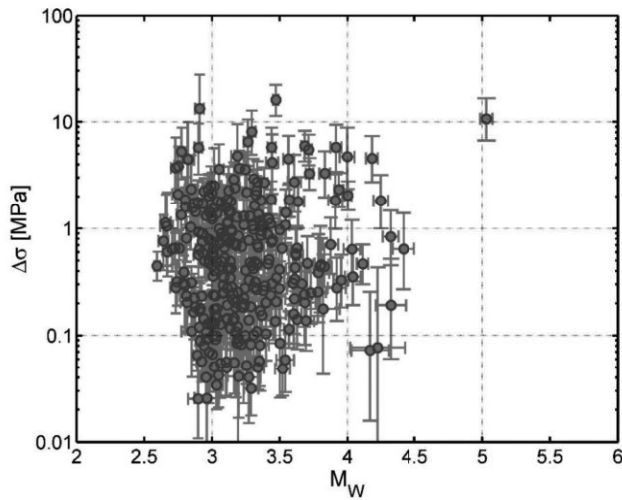
Figure 11. Stress drop versus moment magnitude with the vertical and horizontal error bars. Stress drop values range from 0.02 to16 MPa.
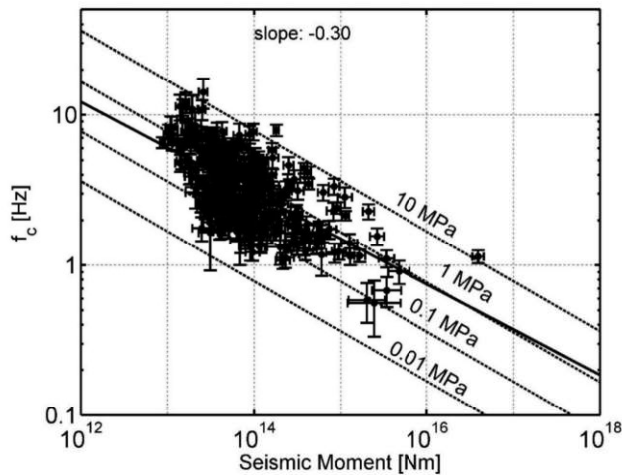

Figure 12. Corner frequency versus seismic moment. Constant stress drop values (dotted lines) and slope of linear fit (solid line) are also shown.

consider high-frequency diminution as site related kappa effect in our study.

To assess the influence of the exponential κ term on the source spectra we evaluate this effect by estimating κ values, independent by its physical meaning, for high-frequency part of each source spectra. The trade-off between corner frequencies and kappa is subject of strong debate. Especially, this problem arises in estimating kappa if the available data set is limited to events below M_L ~3.5. In these cases, separating the influence of kappa, or in any case of the attenuation (in particular near-surface), on the corner-frequency estimation is difficult to be accounted for as discussed by Kilb *et al.* (2012). Since most of our events are larger than M_L 3.5 we set the high-frequency limit f_E to 10 Hz for all source spectra to be reasonably above the corner frequency range of our events (Parolai & Bindi 2004). However, we have also tested $f_E = 12$ Hz to investigate the effect of low-frequency limit (f_E) on source parameters estimation of all events especially for smaller ones. Inspection of source parameter results (e.g. corner frequencies and stress drops) after correcting source spectra for estimated kappa values does not show considerable differences. Therefore, we present the obtained results with $f_E = 10$ Hz. The high-frequency source spectra corrected for

κ are shown in Fig. 8 by white squares with slight discrepancy with the uncorrected spectra at high frequencies demonstrating that κ effect is negligible for the source spectra of our data set. Fig. 9 represents the distribution of calculated κ values. The estimated values are smaller than 0.05 s, which lies in the range typically expected for hard rock sites (Boore 2003; Ktenidou *et al.* 2015) and show a normal distribution with an average of 0.008 s. These small values indicate that the considered reference site, CHTH, does not impose a significant high-frequency diminution effect in the source spectra. However, to provide more in-depth investigation of the kappa effect on station CHTH, we evaluated the kappa values directly from the 223 recorded acceleration spectra at CHTH for the average of two horizontal components. Then, the zero-distance kappa factor was calculated from the best-fit regression line as a first approximation ($\kappa = \kappa_r R + \kappa_0$) to the distribution of kappa values as a function of distances (Anderson & Hough 1984). Fig. 10 shows two examples of the linear fit in a log-linear plot to the acceleration spectra recorded at the reference station CHTH along with a linear regression fit to the distribution of kappa values versus distances as well.

The estimated small value of $\kappa_0 = 0.006$ for station CHTH confirms the fact that the zero-distance kappa factor is negligible and does not affect source spectra considerably as discussed above.

Having determined corner frequencies and seismic moments from the fitting procedure using nonlinear least squares of the source spectra we calculate the stress drop for each event assuming a circular crack model following Keilis-Borok (1959) relation:

$$\Delta\sigma = \frac{7M_0}{16r^3},\tag{8}$$

where r is the source radius in km based on Brune (1970) source model:

$$r = \frac{2.34V_s}{2\pi f_c}.\tag{9}$$

We estimate the radiated S-wave energy from the inverted source spectra using the relation (e.g. Izutani & Kanamori 2001):

$$E_s = \frac{4\pi}{5\rho V_s^5}\int_0^\infty |f\,M(f)|^2\,df.\tag{10}$$

Furthermore, we compute the apparent stress (σ_a) for each event to get more insight on the stress parameters and assessing the relation between stress drop and apparent stress based on ω^2 source model:

$$\sigma_a = \mu\frac{E_s}{M_0},\tag{11}$$

where μ is the rigidity modulus ($\mu = V_s^2.\rho$) and E_s is the radiated S-wave energy obtained from eq. (10).

Fig. 11 depicts the estimated stress drop values ranging from about 0.02 to 16 MPa spanning more than three order of magnitudes as observed in other studies that use large data sets or covering data on regional or global scales (Shearer *et al.* 2006; Allmann & Shearer 2007; Oth *et al.* 2010). The obtained values with an average of 1.1 MPa are comparable with results of crustal earthquakes in Japan (Oth 2013) and the L'Aquila sequence of Italy (Ameri *et al.* 2011) with mean stress drop of 1 MPa and 3 MPa respectively using the same inversion method and source model. In comparison with the recent study in Iran the estimated stress drops are higher than those obtained for Silakhor aftershocks in the Zagros region ranging from 0.04 to 5.3 MPa with an average of 0.9 MPa (Ahmadzadeh *et al.* 2017).

The estimated corner frequency versus seismic moment with the corresponding standard deviations is shown in Fig. 12. Constant stress drop values are indicated by dotted lines. The obtained corner
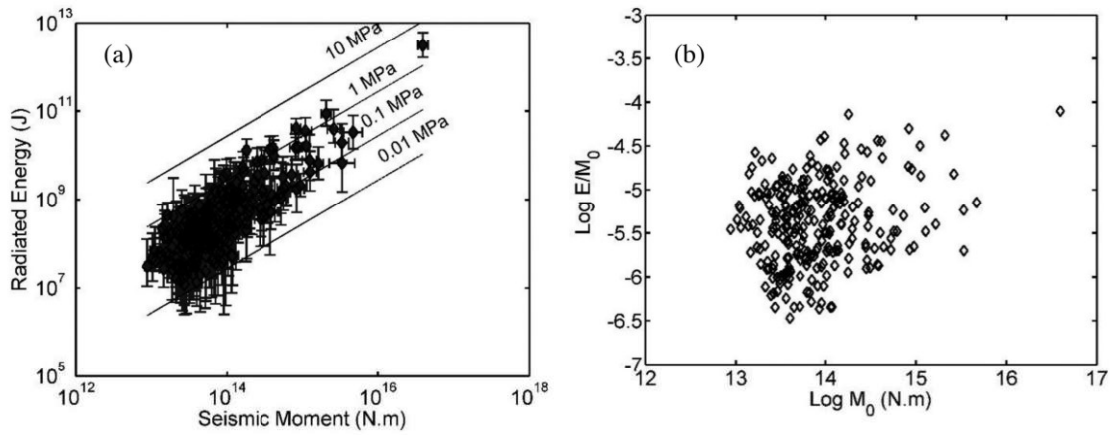
Figure 13. Radiated energy (a) and scaled energy (b) versus seismic moment in the Alborz region.
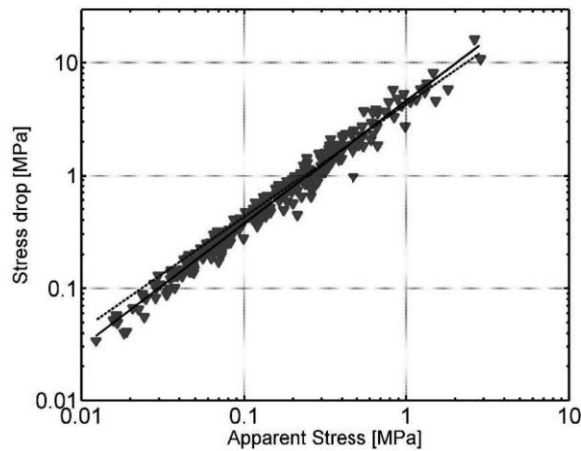

Figure 14. Stress drop versus apparent stress. The best fitted line and the theoretical relation are shown as solid and dashed lines, respectively.

frequencies range from 0.6 to 14 Hz and the seismic moments vary within 4 orders of magnitude, from 10^{13} to 10^{17} Nm. If earthquakes scale self-similarly with seismic moment the stress drop is constant and the relation between moment and corner frequency $M_0 \propto f^{-3}$ (Aki 1967) holds. Thus the slope of a fitted line in Fig. 12 should be close to $-1/3$ that in the case of our data the slope is 0.30 that is fairly consistent with self-similar scaling. The ε parameter introduced by Kanamori & Rivera (2004) to evaluate the deviation from self-similarity takes the value of $\varepsilon = 0.33 \pm 0.22$. Although this value indicates small deviation from self-similarity but it is considerably small in comparison with the reported values from 0.5 to about 1.5 (Mayeda *et al.* 2007; Malagnini *et al.* 2008; Kumar *et al.* 2015) that conclude non self-similar scaling. Even though the distribution of corner frequency versus magnitude is in agreement with the possibility of self-similar scaling, taking into account the narrow magnitude range of this study, we cannot completely exclude non-self-similar scaling.

To get more information on earthquakes source mechanisms and also to assess self-similarity in more details we investigate the radiated and scaled energy and their relation with the seismic moment. Fig. 13(a) represents the evaluated *S*-wave energy versus seismic moment for the selected 312 events. Solid lines represent constant apparent stress values from 0.01 to 10 MPa.

The radiated *S*-wave energy for the events with M_L 3–5.6 range from 10^6 to 10^{12} J and the seismic moments vary in 4 order of

magnitudes from about 10^{13} to 10^{17} Nm. The list of estimated source parameters for all 312 events of this study is presented in Supporting Information Table S1.

The calculated scaled energy, $\tilde{e}$ defined as radiated energy over seismic moment (E/M_0) is shown versus moment in Fig. 13(b). The $\tilde{e}$ values range between 7.9e-05 and 3.4e-07 with the average of 7.4 e-06 J. As can be seen from the figure the scaled energy does not systematically vary with seismic moment. Hence it emphasises the possibility of self-similarity at least in the narrow magnitude range of our data set as reported by other studies (Ide & Beroza 2001; Imanishi & Ellsworth 2006; Viegas *et al.* 2010). However, there are conflicting results in different studies about self-similarity and some studies have reported deviation from self-similarity and non-self-similar scaling especially in energy scaling relationships (e.g. Prejean & Ellsworth 2001; Malagnini *et al.* 2008; Mayeda & Malagnini 2010; Kwiatek *et al.* 2011; Walter *et al.* 2017 among others).

Bandwidth limitation is an important issue that may affect the source parameter estimation especially for small earthquakes. The radiated seismic energy is often subject to underestimation since a broad frequency range spanning up to about ten times the corner frequency is required to estimate 90 per cent of the seismic energy (Ide & Beroza 2001). However, this wide frequency band is not usually available and some studies considered some selection criteria leading to artificial upper limit and trends in stress drop or energy with moment (Abercrombie 1995; Mayeda & Walter 1996; Oth *et al.* 2010). The corner frequency of events in our study with M_L from 3–5.6 range from 0.6 to 14 Hz and the obtained seismic moment vary from 10^{13} Nm to 10^{17} Nm that lays in the range of estimated values worldwide (Boatwright 1994; Pacor *et al.* 2016; Bindi *et al.* 2017; Picozzi *et al.* 2019). Furthermore, the evaluated Brune stress drops and radiated seismic energy, that was found to be of the order of typical values in other studies, implies that bandwidth limitation does not significantly affect our results.

Fig. 14 shows that the evaluated apparent stresses range from about 0.01 to 3 MPa, with a mean value of 0.3 MPa, compared to stress drop values ranging from 0.02 to 16 MPa. According to Singh & Ordaz (1994) it is expected that these parameters theoretically be related as $\Delta\sigma/\sigma_a = 4.3$ considering the ω^2 source model. This relation, however, does not necessarily always hold, and the relationship between apparent stress and stress drop is model-dependent. The best fitted line (solid line) to the stress drop and apparent stress values along with the theoretical relation in the ω^2 case (dashed line) are presented in Fig. 14. As can be seen
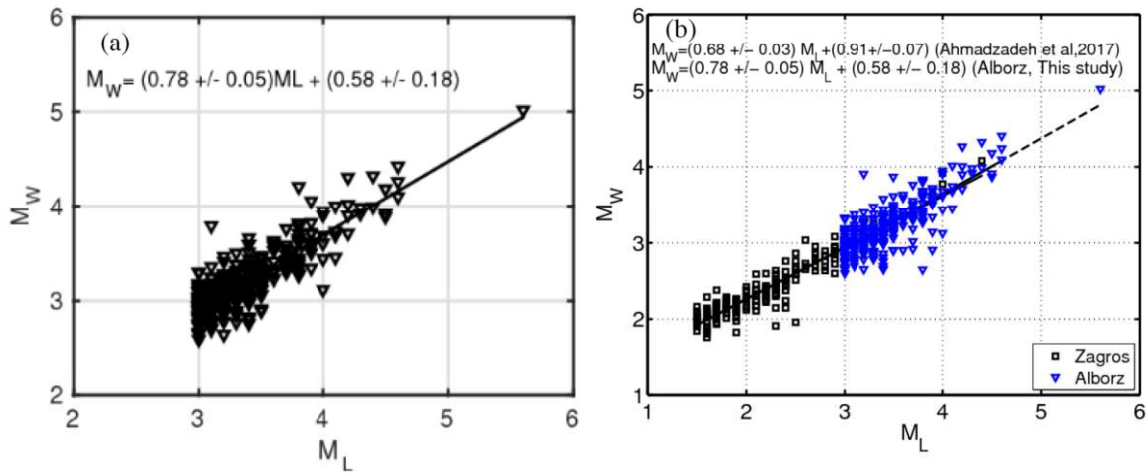
Figure 15. (a) Moment magnitude M_w versus local magnitude M_L estimated from source spectral fitting. The solid line shows the best least-squares fit. (b) Comparison of this study (triangle) with the recent study in Zagros (square) from Ahmadzadeh *et al.* (2017).
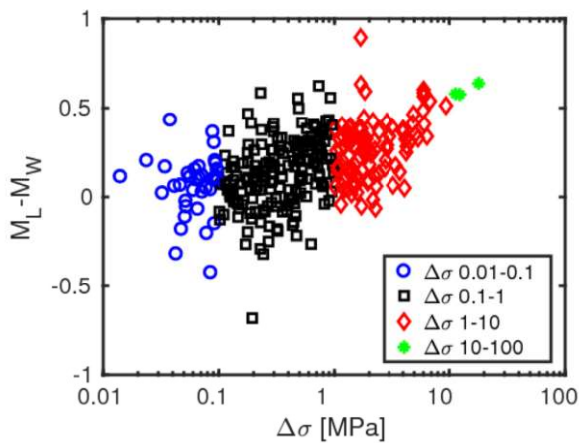

Figure 16. The distribution of M_L–M_w versus stress drops.

from Fig. 14, the results are fairly consistent with this theoretical relation.

Finally, to investigate the relation between the evaluated moment magnitude M_w and local magnitude M_L of our selected events in the Alborz region we have provided a comparison of these two magnitude scales in Fig. 15(a). The obtained M_w in the range of M_w 3–4 is nearly equivalent to the local magnitude M_L. However, for larger events generally M_L values tend to be slightly larger than M_w by about 0.1–0.5 magnitude units. The relationship between M_w and M_L can be expressed as follows using least squares regression:

$$M_w = (0.78 \pm 0.05)\, M_L + (0.58 \pm 0.18). \tag{12}$$

Fig. 15(b) shows the obtained relation for the Alborz in this study in comparison to the result of recent study for the Zagros region (Ahmadzadeh *et al.* 2017) with seismically different characteristics. The observed relationship between M_w and M_L for Alborz is very close to that of the Zagros region and also is in good agreement with previous studies in Iran (e.g. Motaghi & Ghods 2012; Shahvar *et al.* 2013; Zare *et al.* 2014).

Having estimated moment magnitude and stress drop values, the distribution of M_L–M_w versus stress drops shows that the difference of these two magnitude scales slightly increases with increasing stress drop values (Fig. 16).

4.3 Site response

The site response function is obtained from the inversion of FAS for each station within the Alborz region. In addition to perform GIT inversion for horizontal components we obtained the GIT site amplifications for vertical (Z) components to investigate the probable vertical component amplification and its effect on the horizontal to vertical (H/V) spectral ratios. The GIT site responses for vertical component are derived using the same S-wave windows and reference constraint as the horizontal (H) component. Furthermore, we evaluate the site amplification functions using the H/V spectral ratios directly from the observed spectra and compare the results with the aforementioned GIT site responses.

Fig. 17 represents the estimated GIT site responses for horizontal (GIT H) and vertical (GIT Z) components for all stations. The GIT site amplification function ratio of the horizontal and vertical components (GIT H/Z) (solid line) and the H/V spectral ratios (dashed line) are also depicted for comparison. In general, the obtained amplification functions are well constrained with small standard deviations derived from the bootstrap analysis displayed in the GIT H curves as grey shaded areas. It is worth mentioning that all GIT amplification functions are relative to CHTH station that is considered as reference site constraint with significantly flat and near to unity response at all frequencies based on H/V analysis (as can be seen in Fig. 17).

Since the site amplification estimation depends on good azimuthal and distance coverage, reliable site responses can be obtained only when earthquakes are distributed around the station in all directions at different distances (Lermo & Chavez-Garcia 1993; Parolai *et al.* 2004b). In the case of our study most of our stations (e.g. CHTH, DAMV, THKV, GHVR, ASAO, ZNJK, KHMZ and SNGE) recorded large number of events (from a minimum of 50 up to 230 events per station) with good azimuthal and distance coverage. So azimuthal effects, if they exist, may average out in these stations. However, for two other stations (GIDE and NASN), the lack of recorded events may affect the obtained site responses.

As the BIN stations are generally located on bedrock outcrops it is expected that the response functions be nearly flat without considerable amplification and with no obvious predominant frequency peaks in all frequency bands. Considering the GIT H amplification curves in Fig. 17 most stations have almost flat responses without
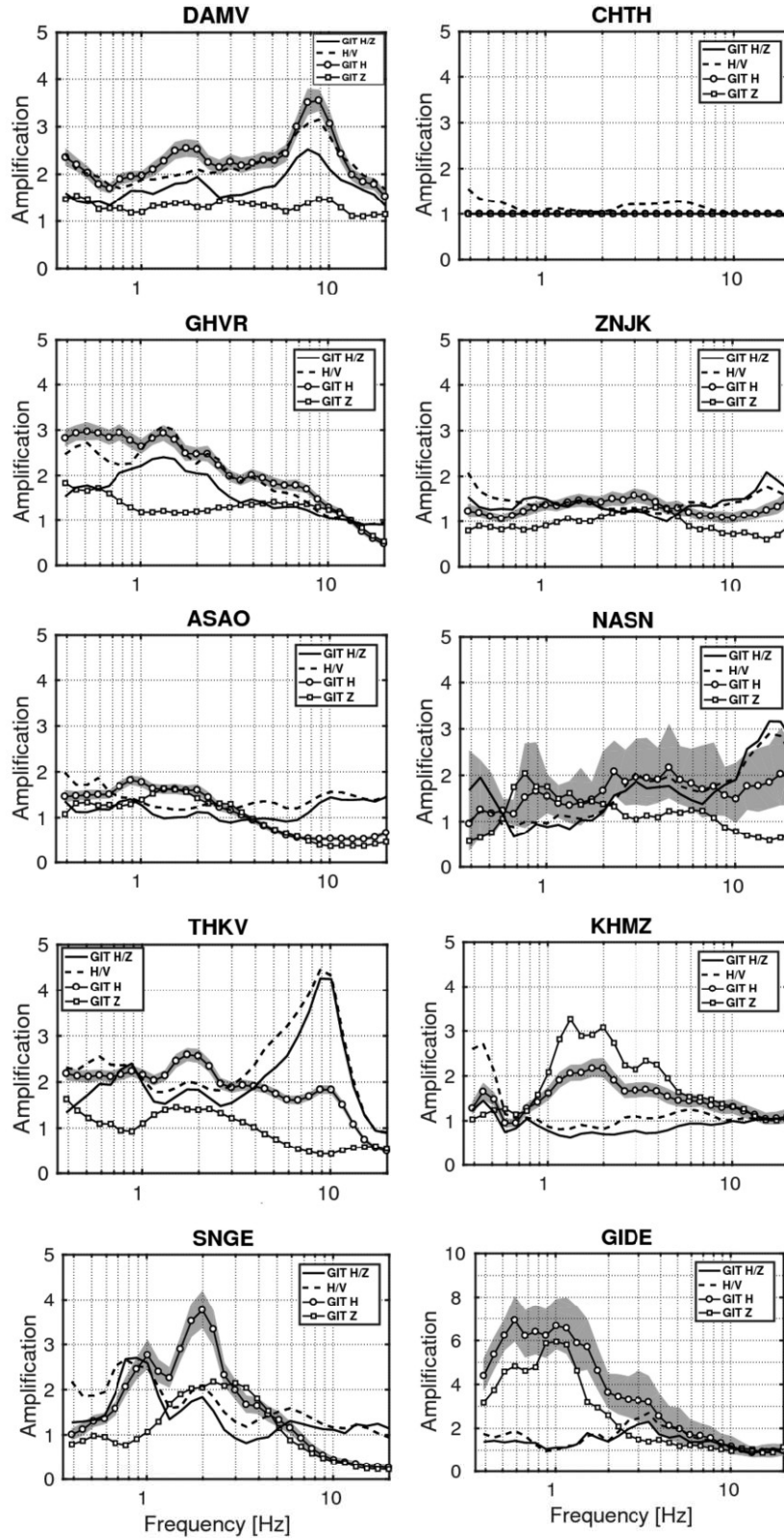
Figure 17. Site response functions resulting from the GIT in comparison with H/V spectral ratios (dashed lines) directly calculated from the observed ground-motion spectra for each station within Alborz. The grey shaded areas mark the mean ± one standard deviation from 100 bootstrap analyses for the GIT H site responses.
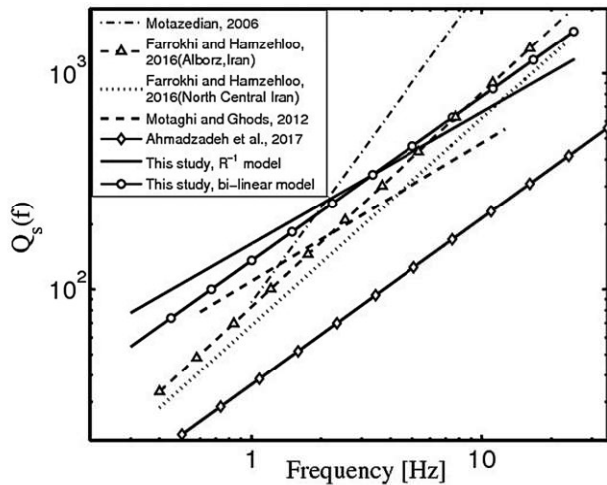
Figure 18. The comparison of the $Q_S(f)$ estimated in this study with other studies for Iran.
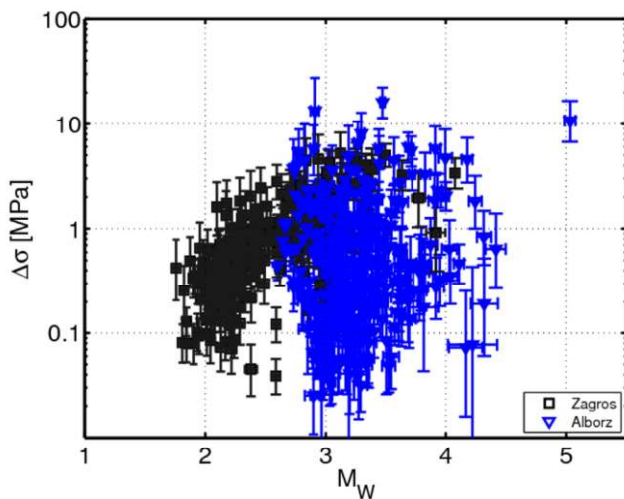

Figure 19. Stress drop variations in terms of moment magnitude for the Alborz in comparison with the Zagros region from Ahmadzadeh *et al.* (2017).

significant amplification and evident dominant frequency peaks. Nevertheless, some stations including DAMV, THKV, SNGE and KHMZ show peak frequencies at 8, 2, 2 and 1 Hz respectively and the maximum amplification is observed at station GIDE with a factor of 7 based on GIT H responses. The overall shape of the GIT H/Z and H/V curves are similar with only slight variations at low frequencies at some stations. However, these functions show considerable discrepancies with GIT H curves in the level of amplification at certain stations.

The evaluated site responses at station DAMV show nearly the same shape with a peak frequency at 8 Hz. This station is located on a limestone outcrop on a narrow ridge with about 100 m above the surrounding area. The stations GHVR and ZNJK also show similar amplifications without any specific dominant frequency. The station ASAO is placed on highly weathered bedrock on a hillside at about 20 m height from the base. The GIT H and GIT Z of this station show the same changes with deamplification at frequencies higher than 3 Hz leading to H/V and GIT H/Z functions nearly around one. The station NASN is positioned on igneous rocks at 2800 m altitude. Site responses indicate complex patterns at frequencies lower than 0.6 Hz and higher than 2 Hz with opposite trends on horizontal

and vertical components in station NASN . This behaviour is likely due to the fractured and weathered rocks around the station. The obtained GIT H at station THKV shows a peak at 2 Hz while the H/V shows a predominant peak at 10 Hz that is due to the deamplification of the GIT Z curve. This station is located on a small hill, at the elevation of 15 m, above a layer of quaternary alluvium of unknown thickness.

The station KHMZ shows high amplitudes on both GIT H and GIT Z above 1 Hz. Therefore, the H/V clearly fails in estimating the site response at this station. The high amplification of the vertical component is likely due to the *S*-to-*P* conversions at the bottom of the existing thin low velocity alluvium layer located on bedrock providing high impedance contrast. The H/V function at station SNGE show a dominant frequency at 1 Hz whereas the GIT H amplifies at 2 Hz. Above 3 Hz both GIT H and GIT Z are deamplified simultaneously leading to unit amplification of H/V and GIT H/Z. This station is located on a hillside with an igneous outcrop 2100 m above the sea level and is near to farmlands with about 100 m higher elevation. The station GIDE is placed 100 km away from the Caspian seashore with 1830 m altitude. This station is installed on an uplifted basin with water saturated surface layers and high topography. The GIT H and GIT Z functions show high amplification of a factor of 7 up to 1.5 Hz after that the curves attenuate to approach unity.

The observed amplification and/or deamplification of the vertical component as can be seen from GIT Z functions at stations ASAO, NASN, THKV, SNGE, KHMZ and GIDE most probably is due to the geological setting and topographical situations. However, a detailed interpretation of the observed amplification functions needs precise information on layering and *S*-wave velocity of the subsurface structures that is not available for these stations and will be certainly a matter of future research efforts.

It is noteworthy that, since the maximum acceleration observed in our study is less than 0.1 g, the deamplification of GIT H and GIT Z functions observed at stations ASAO, SNGE and GIDE at high frequencies are not likely to be related to nonlinearity effects.

5 DISCUSSION AND CONCLUSIONS

We investigated attenuation characteristics, source spectra and site response functions implementing the non-parametric one-step GIT approach to the observed spectral amplitudes of 312 events recorded by BIN in the Alborz region and adjacent area.

The estimated *S*-wave quality factor models show nearly strong frequency dependence and high attenuation characteristics in the Alborz region.

Several studies have been performed to evaluate path attenuation characteristics in various regions of the Iran plateau (e.g. Ma'hood *et al.* 2009; Rahimi *et al.* 2010; Farrokhi *et al.* 2015; Amiri Fard *et al.* 2019). However, only a few of these studies are related to the Alborz region. In the studied region also papers dealing with the analysis of strong motion parameters and attenuation were carried out (e.g. Amiri *et al.* 2007; Bagheri *et al.* 2011; Yazdani *et al.* 2016). We have provided a comparison of the obtained apparent quality factors in this study using R^{-1} and bi-linear geometrical spreading models with other results in Fig. 18 and Table 1.

Motazedian (2006) evaluated the *S*-wave quality factor as $Q_S(f) = 87f^{1.46}$ in Northern Iran based on the vertical component of acceleration records from 22 earthquakes recorded by Building and Housing Research Center stations. Farrokhi & Hamzehloo (2017) determined the attenuation of *P* and *S* waves in Alborz and north central part of Iran using the extended coda normalization method for
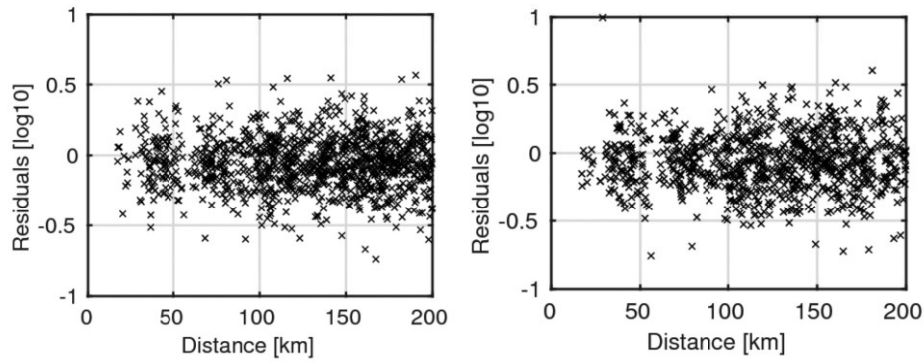
Figure 20. Distribution of residuals versus hypocentral distance at 2.6 Hz (left) and 19.9 Hz (right).
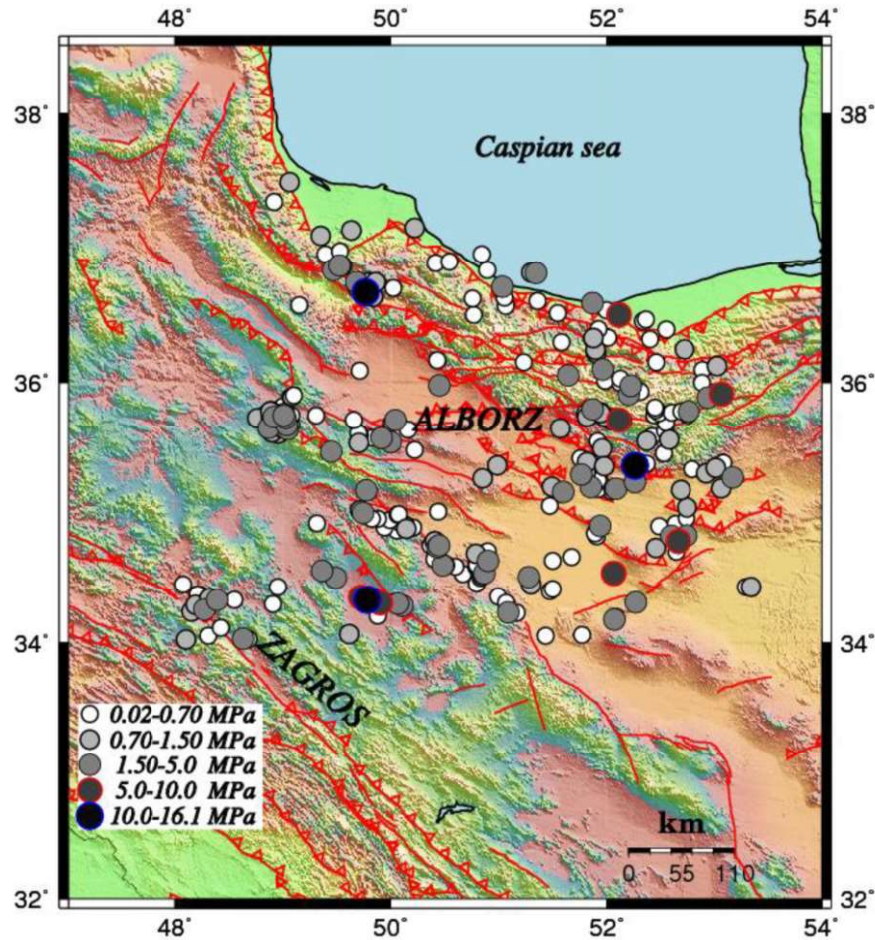

Figure 21. Stress drop values obtained from the GIT inversion for 312 events in the Alborz region and adjacent area.

380 local earthquakes within frequency band 0.4 to 24 Hz. The reported quality factor relations are $Q_S(f) = 83f^{0.99}$ and $Q_S(f) = 68f^{0.96}$ in Alborz and North Central Iran, respectively. Another relation is proposed by Motaghi & Ghods (2012) for direct quality factor Q in the central Alborz as $Q(f) = 109f^{0.64}$ using 136 events recorded at short period stations of the Institute of Geophysics of the University of Tehran during 1996–2007. The estimated S-wave quality factors in our study with both R^{-1} and bi-linear geometrical spreading models are in good agreement with other results in the Alborz region and nearby area. The observed discrepancies between these relations may reflect differences in various methods using different geometrical spreading functions and frequency ranges that lead to

sampling different crustal volumes. We also displayed the recently obtained relation using GIT method for Zagros region (Ahmadzadeh *et al.* 2017) in Fig. 18. As can be seen from this figure the estimated quality factor models for the Zagros region have smaller Q values than the relation for Alborz, indicating that the attenuation of seismic waves in Zagros is higher than the Alborz region. The existing difference between the obtained relations in these two regions can be resulted from the differences in seismotectonic characteristics of these two provinces.

The non-parametric source spectra were fitted using the omega square model to derive earthquake source parameters. The distribution of obtained corner frequencies versus seismic moments implies

Table 1. *S*-wave attenuation models reported for Iran.

Region	Frequency range (Hz)	Quality factor	Geometrical spreading	Reference
Central Alborz	$0.6 \leq f \leq 12$	$Q_S(f) = 109f^{0.6}$	$R^{-1.15}, R < 80$ $R^{-0.09}, 80 \leq R \leq 160$ $R^{-0.5}, R > 160$	Motaghi & Ghods (2012)
Alborz region North Central Iran	Seven frequency bands between $0.4 \leq f \leq 24$	$Q_S(f) = 83\,f^{0.99}$ $Q_S(f) = 68f^{0.96}$	$R^{-1}, R < 90$ $(90\,R)^{-0.5}, R \geq 90$	Farrokhi & Hamzehloo (2017)
North of Iran	$1 < f \leq 10$	$Q_S(f) = 87f^{1.46}$	$R^{-0.6}, R < 70$ $R^{0.2}, 70 \leq R \leq 150$ $R^{-0.1}, R > 150$	Motazedian (2006)
Zagros region	$0.5 \leq f \leq 35$	$Q_S(f) = 36f^{0.77}$	$(R_0/R)^{-1}$	Ahmadzadeh *et al.* (2017)
Alborz region	$0.3 < f \leq 20$	$Q_S(f) = 162f^{0.61}$ $Q_S(f) = 136f^{0.76}$	$(R_0/R)^{-1}\ R < 100$ $(R_0/R)^{-1}\ R < 70$ $(R_0/70)^{-1}(70/R)^{-1.4}$ $70 \leq R < 100$	This study

the possibility of self-similar scaling for our data set, although we acknowledge that the fairly small magnitude range of our study prevents a definite conclusion about the source scaling. The stress drop values range from about 0.02 to 16 MPa with an average of 1.1 MPa. The inferred stress drops are relatively small in comparison with typically observed values worldwide (~0.1–100, e.g. Kanamori 1994). In comparison with the recent study in Iran for Silakhor aftershocks (Ahmadzadeh *et al.* 2017), the stress drop values estimated for the Alborz region show higher variability (for the same magnitude range) and reach larger values than in the Zagros region (Fig. 19). The estimated higher stress drops for the Alborz region are expected considering the seismotectonic characteristics of this province located far away from plate boundaries in comparison with interplate Zagros region. This result is compatible with other studies worldwide considering the tectonic setting of study areas (e.g. Allmann & Shearer 2009; Oth & Kaiser 2014). However, considering the variety of structures in our study area further works are required to derive more details about the relation of stress drops with tectonic structures based on intensive seismic network data set in this region.

We compared the estimated stress drops with the evaluated apparent stress values assuming the omega square model. The obtained relation between these two parameters is reasonably consistent with the theoretically expected relation.

Comparison of estimated M_w versus local magnitude M_L indicates that M_w and M_L are linearly correlated and almost equivalent in the range of M_w 3–4. However, for larger events generally M_w estimates are smaller than M_L values by about 0.1–0.5 magnitude units. The obtained relation is in good agreement with a few available studies for Iran (Shahvar *et al.* 2013; Zare *et al.* 2014; Ahmadzadeh *et al.* 2017). It is noteworthy that site amplification could affect M_L estimates leading to observed discrepancies between M_L and M_w (Fig. 15b). Recently, IIEES has started to revise the local magnitude scale for Iran plateau to consider station corrections since 2017. However, comparing new M_L scale considering station corrections with previous ones that we used in this study show only about 0.1–0.2 differences in M_L values.

The high-frequency kappa values were estimated from the high-frequency part of each source spectra. The calculated κ values with small mean value of 0.008 sec indicate that the high-frequency κ decay only slightly affects the source spectra and this effect, if present, has been taken up absolutely by the attenuation term.

There are some uncertainties in the earthquake source and propagation parameters due to the simplifications underlying the selected spectral modelling. These uncertainties may arise from different factors including model assumptions (e.g. differences with respect to the selected source model, path functions like geometrical spreading and quality factor function, constant *S*-wave velocity and assumed straight line ray path), the existing trade-offs between different parameters (such as trade-off between *S*-wave quality factor Q and geometrical spreading, source terms and near source attenuation, or between source and site effects) and bandwidth limitations. To appreciate the effect of the model simplification we computed the residuals as the observed minus predicted spectral values.

The distribution of the residuals is shown in Fig. 20 as an example for two selected frequencies of 2.6 and 19.9 Hz. The residuals vary around zero and do not show any trend with distance demonstrating that the non-parametric inversion provides a good representation of the observed recordings considered in this study. Of course this still not a guarantee that trade-offs between the parameters is not happening. Furthermore, we would like to stress once more that the parameter values are valid in the context of the adopted models and care should be taken when comparisons with absolute values of parameters obtained under different assumptions are done.

Considering the tectonic setting, the area we are investigating is likely to show lateral and vertical heterogeneities. The model we are using assumes the propagation of waves in a homogeneous model. It follows that the obtained results will only represent average characteristics of the whole investigated crustal volume. This simplification of the assumption might in turn affect the source parameter estimation as one of the main origins of uncertainties as discussed above. However, since an investigation of the source parameters spatial distribution (as shown in Fig. 21 for estimated stress drops) is not indicating any significant pattern, we think that the approximation done is valid at first order. Future studies will focus on better estimating local properties of the medium that could improve the source parameter estimation.

The obtained site amplification functions from GIT are nearly flat with no obvious predominant frequency peaks for most stations as expected for rock stations. However, a few stations represent the amplification peaks almost range from 1 to about 8 Hz with the maximum amplification of about 7 with respect to the reference site. The observed amplification or deamplification of vertical component provided by GIT Z functions at specific stations result in differences of the H/V amplitude in comparison with the GIT H amplification curves. The weathered and fractured layers near the surface as well as topographical conditions and the existing

impedance contrasts can be linked to the observed high amplification effects of vertical component.

The obtained results of this work on source parameters, path attenuation and site effects provide important elements to predict and simulate reliable earthquake ground motion and seismic hazard assessment particularly in the Alborz region with multiple populated cities including the capital Tehran.

REFERENCES

Abbassi, A., Nasrabadi, A., Tatar, M., Yaminifard, F., Abbassi, M.R., Hatzfeld, D. & Priestley, K., 2010. Crustal velocity structure in the southern edge of the Central Alborz (Iran), *J. Geodyn.,* **49,** 68–78.

Abercrombie, R.E., 1995. Earthquake source scaling relationships from −1 to 5 M_L using seismograms recorded at 2.5 km depth, *J. geophys. Res.,* **100,** 24 015–24 036.

Ahmadzadeh, S., Parolai, S., Javan-Doloei, G. & Oth, A., 2017. Attenuation characteristics, source parameters and site effects from inversion of S waves of the March 31, 2006 Silakhor aftershocks in Western Iran, *Ann. Geophys.,* **60**(6 Sup), SE668.

Aki, K., 1967. Scaling law of seismic spectrum, *J. geophys. Res.,* **72,** 1217–1231.

Alavi, M., 1996. Tectonostratigraphic synthesis and structural style of the Alborz mountain system in northern Iran, *J. Geodyn.,* **21,** 1–33.

Allen, M.B., Ghassemi, M.R., Shahrabi, M. & Qorashi, M., 2003. Accommodation of late Cenozoic oblique shortening in the Alborz range, northern Iran, *J. Struct. Geol.,* **25,** 659–672.

Allmann, B.P. & Shearer, P.M., 2007. Spatial and temporal stress drop variations in small earthquakes near Parkfield, California, *J. geophys. Res.,* **112,** B04305.

Allmann, B.P. & Shearer, P.M., 2009. Global variations of stress drop for moderate to large earthquakes, *J. geophys. Res.,* **114,** B01310.

Ambraseys, N.N & Melville, C.P., 1982. *A History of Persian Earthquakes,* Cambridge Univ. Press, p. 219.

Ameri, G., Oth, A., Pilz, M., Bindi, D., Parolai, S., Luzi, L., Mucciarelli, M. & Cultrera, G., 2011. Separation of source and site effects by generalized inversion technique using the aftershock recordings of the 2009 L'Aquila earthquake, *Bull. Earthq. Eng.,* **9,** 717–739.

Amiri Fard, R., Javan Doloei, G., Rahimi, H. & Farrokhi, M., 2019. Attenuation of P and S waves in Western part of Iran, *Geophys. J. Int.* **218,** 1143–1156.

Amiri, G.G., Mahdavian, A. & Dana, F. M., 2007. Attenuation relationships for Iran, *J. Earthq. Eng.,* **11,** 469–492.

Anderson, J.G., 1991. A preliminary descriptive model for the distance dependence of the spectral decay parameter in southern California, *Bull. seism. Soc. Am.,* **81,** 2186–2193.

Anderson, J.G. & Hough, S.E., 1984. A model for the shape of the Fourier amplitude spectrum of acceleration at high frequencies, *Bull. seism. Soc. Am.,* **74,** 1969–1993.

Andrews, D.J., 1986. Objective determination of source parameters and similarity of earthquakes of different size, in *Earthquake Source Mechanics,* pp. 259–268, eds Das, S., Boatwright, J. & Scholz, C.H., AGU.

Bagheri, A., Amiri, G.G., Khorasani, M. & Haghdoust, J., 2011. Determination of attenuation relationships using an optimization problem, *Int. J. Optim. Civil Eng.,* **4,** 597–607.

Berberian, M., 1976. Contribution to the seismotectonics of Iran (Part II), Report No. 39, Geological Survey of Iran.

Berberian, M., Qorashi, M., Jackson, J.A., Priestley, K. & Wallace, T., 1992. The Rudbar-Tarom earthquake of 20 June 1990 in NW Persia: preliminary field and seismological observations, and its tectonic significance, *Bull. seism. Soc. Am.,* **82,** 1726–1755.

Berberian, M. & Yeats, R.S., 1999. Patterns of historical earthquake rupture in the Iranian Plateau, *Bull. seism. Soc. Am.,* **89,** 120–139.

Bindi, D., Luzi, L., Pacor, F., Franceschina, G. & Castro, R.R., 2006. Ground-motion prediction from empirical attenuation relationships versus recorded data: the case of the 1997–1998 Umbria-Marches, Central Italy, strong motion data set, *Bull. seism. Soc. Am.,* **96,** 984–1002.

Bindi, D., Spallarossa, D. & Pacor, F., 2017. Between-event and between station variability observed in the Fourier and response spectra domains: comparison with seismological models, *Geophys. J. Int.,* **210,** 1092–1104.

Boatwright, J., 1994. Regional propagation characteristics and source parameters of earthquakes in northeastern North America, *Bull. seism. Soc. Am.,* **84**(1), 1–15.

Bonilla, L.F., Steidl, J.H., Lindley, G.T., Tumarkin, A.G. & Archuleta, R.J., 1997. Site amplification in the San Fernando Valley, California: variability of site-effect estimation using the S-wave, coda, and H/V, *Bull. seism. Soc. Am.,* **87,** 710–730.

Boore, D.M., 1983. Stochastic simulation of high-frequency ground motions based on seismological models of the radiated spectra, *Bull. seism. Soc. Am.,* **73,** 1865–1894.

Boore, D.M., 2003. Simulation of ground motion using the stochastic method, *Pure appl. Geophys.,* **160,** 635–676.

Boore, D.M. & Boatwright, J., 1984. Average body-wave radiation coefficients, *Bull. seism. Soc. Am.* **74,** 1615–1621.

Brune, J.N., 1970. Tectonic stress and the spectra from seismic shear waves earthquakes, *J. geophys. Res.,* **75,** 4997–5009.

Brune, J.N., 1971. Correction, *J. geophys. Res.,* **76,** 5002.

Castro, R.R., Andersom, J.G. & Singh, S.K., 1990. Site response, attenuation and source spectra of S waves along the Guerrero, México, subduction zone, *Bull. seism. Soc. Am.,* **80,** 1481–1503.

Castro, R.R., Massa, M., Augliera, P. & Pacor, F., 2008. Body wave attenuation in the region of Garda, Italy, *Pure appl. Geophys.,* **165,** 1351–1366.

Castro, R.R., Pacor, F., Puglia, R., Ameri, G., Letort, J., Massa, M. & Luzi, L., 2013. The 2012 May 20 and 29, Emilia earthquakes (Northern Italy) and the main aftershocks: S wave attenuation, acceleration source functions and site effects, *Geophys. J. Int.,* **195,** 597–611.

Doloei, J.G. & Roberts, R., 2003. Crust and uppermost mantle structure of Tehran region from analysis of teleseismic P-waveform receiver functions, *Tectonophysics,* **364,** 115–133.

Donner, S., Krüger, F., Rößler, D. & Ghods, A., 2014. Combined Inversion of broadband and short-period waveform data for regional moment tensors: a case study in the Alborz mountains, Iran, *Bull. seism. Soc. Am,* **104,** 1358–1373.

Donner, S., Rößler, D., Krüger, F., Ghods, A. & Strecker, M. R., 2013. Segmented seismicity of the M_w 6.2 Baladeh earthquake sequence (Alborz Mountains, Iran) revealed from regional moment tensors, *J. Seismol.,* **17,** 925–959.

Drouet, S., Souriau, A. & Cotton, F., 2005. Attenuation, seismic moment, and site effects for weak-motion events: application to the Pyrenees, *Bull. seism. Soc. Am.,* **95,** 1731–1748.

Dutta, U., Biswas, N., Martirosyan, A., Papageorgious, A. & Kinoshita, S., 2003. Estimation of earthquake source parameters and site response in Anchorage, Alaska from strong-motion network data using generalized inversion method, *Phys. Earth planet. Inter.,* **137,** 13–29.

Edwards, B., Rietbrock, A., Bommer, J.J. & Baptie, B., 2008. The acquisition of source, path and site effects from micro-earthquake recordings using Q tomography: application to the United Kingdom, *Bull. seism. Soc. Am.,* **98**(4), 1915–1935.

Efron, B., 1979. Bootstrap methods, another look at the jacknife, *Ann. Stat.,* **7,** 1–26.

Farrokhi, M. & Hamzehloo, H., 2017. Body wave attenuation characteristics in the crust of Alborz region and North Central Iran, *J. Seismol.,* **21,** 631–646.

Farrokhi, M., Hamzehloo, H., Rahimi, H. & Allamehzadeh, M., 2015. Estimation of coda-wave attenuation in the central and eastern Alborz, Iran, *Bull. seism. Soc. Am,* **105,** 1756–1767.

Fernández-Heredia, A.I., Huerta-Lopez, C.I., Castro-Escamilla, R.R. & Romo-Jones, J., 2012. Soil damping and site dominant vibration period determination, by means of random decrement method and its relationship with the site-specific spectral decay parameter kappa, *Soil Dyn. Earthq. Eng.,* **43,** 237–246.

Haghshenas, E., Bard, P.-Y. & Theodulis, N., 2008. Empirical evaluation of microtremor H/V spectral ratio, *Bull. Earthq. Eng.,* **6,** 75–108.

Hutton, L.K. & Boore, D.M., 1987. The M_L scale in Southern California, *Bull. seism. Soc. Am,* **77**(6), 2074–2094.

Ide, S. & Beroza, G.C., 2001. Does apparent stress vary with earthquake size?, *Geophys. Res. Lett.,* **28,** 3349–3352.

Imanishi, K. & Ellsworth, W.L., 2006. Source scaling relationships of microearthquakes at Parkfield, CA, determined using the SAFOD Pilot Hole Seismic Array, in *Earthquakes: Radiated Energy and the Physics of Faulting,* Geophys. Monogr. Ser., Vol.170, pp. 81–90, eds Abercrombie, R. et al., AGU.

Izutani, Y. & Kanamori, H., 2001. Scale-dependence of seismic energy-to-moment ratio for strike-slip earthquakes in Japan, *Geophys, Res. Lett.,* **28,** 4007–4010.

Jackson, J.A., Priestley, K., Allen, M. & Berberian, M., 2002. Active tectonics of the South Caspian Basin, *Geophys. J. Int.,* **148,** 214–245.

Kanamori, H., 1994. Mechanics of earthquakes, *Annu. Rev. Earth Planet. Sci.,* **22,** 207–237.

Kanamori, H. & Rivera, L., 2004. Static and dynamic scaling relations for earthquakes and their implications for rupture speed and stress drop, *Bull. seism. Soc. Am.,* **94,** 314–319.

Keilis-Borok, V., 1959. On the estimation of the displacement in an earthquake source and of source dimension, *Ann. Geophys.,* **12,** 205–214.

Kilb, D., Biasi, G., Anderson, J.G., Brune, J., Peng, Z. & Vernon, F.L., 2012. A comparison of spectral parameter kappa from small and moderate earthquakes using Southern California ANZA Seismic Network Data, *Bull. seism. Soc. Am.,* **102,** 284–300.

Konno, K. & Ohmachi, T., 1998. Ground-motion characteristics estimated from spectral ratio between horizontal and vertical components of microtremors, *Bull. seism. Soc. Am.,* **88,** 1228–1241.

Ktenidou, O.-J., Abrahamson, N.A., Drouet, S. & Cotton, F., 2015. Understanding the physics of kappa (κ): insights from a downhole array, *Geophys. J. Int.* **203,** 678–691.

Ktenidou, O.-J., Cotton, F., Abrahamson, N.A. & Anderson, J.G., 2014. Taxonomy of κ: a review of definitions and estimation approaches targeted to applications, *Seismol. Res. Lett.,* **85**(1), 135–146.

Kumar, M., Yallanki, S., Biswas, K. & Mandal, P., 2015. Evidence for non-self-similarity in the M_w 7.7 2001 Bhuj earthquake sequence, *Nat. Hazards,* **75,** 1577–1598.

Kwiatek, G., Plenkers, K., Dresen, G. & Group, J.R., 2011. Source parameters of picoseismicity recorded at Mponeng deep gold mine, South Africa: implications for scaling relations, *Bull. seism. Soc. Am.,* **101,** 2592–2608.

Lermo, J. & Chavez-Garcia, F.J., 1993. Site effect evaluation using spectral ratios with only one station, *Bull. seism. Soc. Am.,* **83,** 1574–1594.

Ma'hood, M., Hamzehloo, H. & Doloei, G., 2009. Attenuation of high frequency *P* and *S* waves in the crust of the East-Central Iran, *Geophys. J. Int.,* **179**(3), 1669–1678.

Malagnini, L., Scognamiglio, L., Mercuri, A., Akinci, A. & Mayeda, K., 2008. Strong evidence for non-similar earthquake source scaling in central Italy, *Geophys. Res. Lett.,* **35,** L17303.

Mayeda, K & Walter, W.R., 1996. Moment, energy, stress drop and source spectra of Western U.S. earthquakes from regional coda envelopes, *J. geophys. Res.,* **101,** 11 195–11 208.

Mayeda, K. & Malagnini, L., 2010. Source radiation invariant property of local and near-regional shear-wave coda: application to source scaling for the M_w 5.9 Wells, Nevada Sequence, *Geophys. Res. Lett.,* **37,** L07306.

Mayeda, K., Malagnini, L. & Walter, W.R., 2007. A new spectral ratio method using narrow band coda envelopes: evidence for non-self-similarity in the Hector Mine sequence, *Geophys. Res. Lett.,* **34,** L11303.

Mirzaei, N., Mengtan, G. & Yuntai, C., 1998. Seismic source regionalization for seismic zoning of Iran: major seismotectonic provinces, *J. Earthq. Pred. Res.,* **7,** 465–495.

Motaghi, K. & Ghods, A., 2012. Attenuation of ground-motion spectral amplitudes and its variations across the Central Alborz Mountains, *Bull. seism. Soc. Am.,* **102,** 1417–1428.

Motazedian, D., 2006. Region-specific key seismic parameters for earthquakes in northern Iran, *Bull. seism. Soc. Am.,* **96,** 1383–1395.

Nakamura, Y., 1989. A method for dynamic characteristics estimation of subsurface using microtremor on the ground surface, *Q. Rep. Railw. Tech. Res. Inst.,* **30,** 25–33.

Nowroozi, A., 1976. Seismotectonic provinces of Iran, *Bull. seism. Soc. Am.,* **66,** 1249–1276.

Oth, A., 2013. On the characteristics of earthquake stress release variations in Japan, *Earth planet. Sci. Lett.,* **377,** 132–141.

Oth, A., Bindi, D., Parolai, D. & Di Giacomo, D. 2010. Earthquake scaling characteristics and the scale-(in)dependence of seismic energy-to-moment ratio: insights from KiK-net data in Japan, *Geophys. Res. Lett.,* **37,** L19304.

Oth, A., Bindi, D., Parolai, S. & Giacomo, D.D., 2011. Spectral analysis of K-NET and KiK-net data in Japan, part II: on attenuation characteristics, source spectra, and site response of borehole and surface stations, *Bull. seism. Soc. Am.,* **101,** 667–687.

Oth, A. & Kaiser, A.E., 2014. Stress release and source scaling of the 2010–2011 Canterbury, New Zealand, earthquake sequence from spectral inversion of ground motion data, *Pure appl. Geophys.,* **171,** 2767–2782.

Oth, A., Parolai, S., Bindi, D. & Wenzel, F., 2009. Source spectra and site response from *S* waves of intermediate-depth Vrancea, Romania, earthquakes, *Bull. seism. Soc. Am.,* **99,** 235–254.

Pacor, F. et al., 2016. Spectral models for ground motion prediction in the L'Aquila region (Central Italy): evidence for stress drop dependence on magnitude and depth, *Geophys. J. Int.,* **204,** 716–737.

Paige, C.C. & Saunders, M.A., 1982. LSQR: an algorithm for sparse linear equations and sparse least squares, *ACM Trans. Math. Softw.,* **8,** 195–209.

Parolai, S. & Bindi, D., 2004. Influence of soil-layer properties on k evaluation, *Bull. seism. Soc. Am.,* **94,** 349–356.

Parolai, S., Bindi, D., Ansal, A., Kurtulus, A., Strollo, A. & Zschau, J., 2010. Determination of shallow *S*-wave attenuation by down-hole waveform deconvolution: a case study in Istanbul (Turkey), *Geophys. J. Int.,* **181,** 1147–1158,

Parolai, S., Bindi, D. & Augliera, P., 2000. Application of the generalized inversion technique (GIT) to a microzonation study: numerical simulations and comparison with different site estimation techniques, *Bull. seism. Soc. Am.,* **90,** 286–297.

Parolai, S., Bindi, D., Baumbach, M., Grosser, H., Milkereit, C., Karakisa, S. & Zunbul, S., 2004a. Comparison of different site response estimation techniques using aftershocks of the 1999 Izmit earthquake, *Bull. seism. Soc. Am.,* **94,** 1096–1108.

Parolai, S., Richwalski, S.M., Milkereit, C. & Bormann, P., 2004b. Assessment of the stability of H/V spectral ratios and comparison with earthquake data in the Cologne area (Germany), *Tectonophysics,* **390,** 57–73.

Petukhin, A.G., Gusev, A.A., Guseva, E.M., Gordeev, E.I. & Chebrov, V.N., 1999. Preliminary model for scaling of Fourier spectra of strong ground motion recorded on Kamchatka, *Pure appl. Geophys.,* **156,** 445–468.

Picozzi, M., Bindi, D., Spallarossa, D., Oth, A., Di Giacomo, D. & Zollo, A., 2019. Moment and energy magnitudes: diversity of views on earthquake shaking potential and earthquake statistics, *Geophys. J. Int.,* **216,** 1245–1259.

Pilz, M., Parolai, S., Leyton, F., Campos, J. & Zschau, J., 2009. A comparison of site response techniques using earthquake data and ambient seismic noise analysis in the large urban areas of Santiago de Chile, *Geophys. J. Int.,* **178,** 713–728.

Prejean, S.G. & Ellsworth, W.L., 2001. Observations of earthquake source parameters and attenuation at 2 km depth in the Long Valley Caldera, eastern California, *Bull. seism. Soc. Am.,* **91,** 165–177.

Purvance, M.D. & Anderson, J.G., 2003. A comprehensive study of the observed spectral decay in strong-motion accelerations recorded in Guerrero, Mexico, *Bull. seism. Soc. Am.,* **93,** 600–611.

Radjaee, A., Rham, D., Mokhtari, M., Tatar, M., Priestley, K. & Hatzfeld, D., 2010. Variation of Moho depth in the central part of the Alborz Mountains, northern Iran, *Geophys. J. Int.,* **181,** 173–184.

Rahimi, H., Motaghi, K., Mukhopadhyay, S. & Hamzehloo, H. 2010. Variation of coda wave attenuation in Alborz region and Central Iran, *Geophys. J. Int.,* **181,** 1643–1654.

Shahvar, M., Zare, M. & Castellaro, S., 2013. A unified seismic catalog for the Iranian Plateau (1900–2011), *Seismol. Res. Lett.,* **84,** 233–249.

Shearer, P., Prieto, G. & Hauksson, E., 2006, Comprehensive analysis of earthquake source spectra in southern California, *J. geophys. Res.,* **111,** B06303.

Singh, S.K. & Ordaz, M., 1994. Seismic energy release in Mexican subduction zone earthquakes, *Bull. seism. Soc. Am.,* **84,** 1533–1550.

Sokolov, V., Bonjer, K.-P., Oncescu, M. & Rizescu, M., 2005. Hard rock spectral models for intermediate depth Vrancea (Romania) earthquakes, *Bull. seism. Soc. Am.,* **95,** 1749–1765.

Stocklin, J., 1968. Structural history and tectonic of Iran: a review, *AAPG Bull.,* **52,** 1229–1258.

Tatar, M., Jackson, J., Hatzfeld, D. & Bergman, E., 2007. The 2004 May 28 Baladeh earthquake (M_w6.2) in the Alborz, Iran: overthrusting the south Caspian margin, partitioning of oblique convergence and the seismic hazard of Tehran, *Geophys. J. Int.,* **170,** 249–261.

Tsuda, K., KoKestsu, K., Hisada, Y. & Hayakawa, T., 2010. Inversion analysis of site responses in the Kanto basin using data from a dense strong motion seismograph array, *Bull. seism. Soc. Am.,* **100,** 1276–1287.

Vernant, P. *et al.*, 2004. Deciphering oblique shortening of central Alborz in Iran using geodetic data, *Earth planet. Sci. Lett.,* **223,** 177–185.

Viegas, G., Abercrombie, R.E. & Kim, W.-Y., 2010. The 2002 M5 Au Sable Forks, NY, earthquake sequence: source scaling relationships and energy budget, *J. geophys. Res.,* **115,** B07310.

Walter, W.R., Yoo, S.-H., Mayeda, K. & Gök, R., 2017. Earthquake stress via event ratio levels: application to the 2011 and 2016 Oklahoma seismic sequences, *Geophys. Res. Lett.,* **44,** 3147–3155.

Wang, H.W., Ren, Y.F. & Wen, R.Z., 2018. Source parameters, path attenuation, and site effects from strong-motion recordings of the Wenchuan aftershocks (2008–2013) using nonparametric generalized inversion technique, *Geophys. J. Int.* **212,** 872–890.

Yazdani, A., Kowsari, M. & Amani, S., 2016. Development of a regional attenuation relationship for Alborz, Iran, *J. Earth Space Phys.,* **41,** 39–50.

Yenier, E. & Atkinson, G.M., 2015. Regionally adjustable generic ground-motion prediction equation based on equivalent point source simulations: application to central and eastern North America, *Bull. seism. Soc. Am.,* **105,** 1989–2009.

Zafarani, H., Hassani, B. & Ansari, A., 2012. Estimation of earthquake parameters in the Alborz seismic zone, Iran using generalized inversion method, *Soil Dyn. Earthq. Eng.,* **42,** 197–218.

Zare, M. *et al.*, 2014. Recent developments of the Middle East catalog, *J. Seismol.,* **18,** 749–772.

SUPPORTING INFORMATION

Supplementary data are available at *GJI* online.

Table S1. List of source parameters including moment magnitude (M_w), seismic moment (M_0), corner frequency (f_c), stress drop ($\Delta\sigma$) and radiated energy (E_s) estimated from the inversion of *S*-wave spectra for the Alborz region.

Please note: Oxford University Press is not responsible for the content or functionality of any supporting materials supplied by the authors. Any queries (other than missing material) should be directed to the corresponding author for the paper.